

DESIGN AND NUMERICAL INVESTIGATIONS OF A COUNTER-ROTATING AXIAL COMPRESSOR
FOR A GEOTHERMAL POWER PLANT APPLICATION

By

Thomas Qualman II

A THESIS

Submitted to
Michigan State University
in partial fulfillment of the requirements
for the degree of

Mechanical Engineering – Master of Science

2013

ABSTRACT

DESIGN AND NUMERICAL INVESTIGATIONS OF A COUNTER-ROTATING AXIAL COMPRESSOR FOR A GEOTHERMAL POWER PLANT APPLICATION

By

Thomas Qualman II

Geothermal provides a steady source of energy unlike other renewable sources, however, there are non-condensable gases (NCG's) that need to be removed before the steam enters the turbine/generator or the efficiency suffers. By utilizing a multistage counter-rotating axial compressor with integrated composite wound impellers the process of removing NCG's could be significantly improved. The novel composite impeller design provides a high level of corrosion resistance, a good strength to weight ratio, reduced size, and reduced manufacturing and maintenance costs. This thesis focuses on the design of the first 3 stages of a multistage counter-rotating axial compressor with integrated composite wound impellers for NCG removal. Because of the novel technique, an unusual set of constraints required a simplified 1 and 2D design methodology to be developed and investigated through CFD. The results indicate that by utilizing constant thickness blades with constant shroud radius (to ease manufacturing difficulties) a total pressure ratio of 1.37 with a total polytropic efficiency of 89.81% could be achieved.

ACKNOWLEDGEMENTS

First, I would really like to thank my thesis advisor, Dr. Mueller, for all the support and guidance he has given me since our paths first crossed when I was just a lowly undergraduate student. A special thanks also goes out to Dr. Engeda and Dr. Wichman for both being on my committee as well as for their encouragement over the years. I would also like to thank my friend and colleague Blake Gower for all his help.

TABLE OF CONTENTS

LIST OF TABLES.....	vi
LIST OF FIGURES.....	vii
KEY TO ABBREVIATIONS.....	ix
CHAPTER 1.0	1
1.1 Introduction to Geothermal Power Plants	1
1.2 Issue of NCG Removal and Current Methods.....	3
1.3 Proposed Improvement.....	4
CHAPTER 2.0	7
2.1 Introduction of COSO Application	7
2.2 COSO Benchmark Design	9
2.3 Scope of Work.....	10
CHAPTER 3.0	12
3.1 Introduction of Simple 1D Design	12
3.2 Axial Compressor Basics	13
3.3 1D Counter-Rotating Axial Compressor Design Methodology	19
CHAPTER 4.0	27
4.1 Introduction of Simple 2D Design	27
4.2 2D Counter-Rotating Axial Compressor Design Methodology	27
CHAPTER 5.0	31
5.1 Introduction to CFD	31
5.2 Compressor Modeling for CFD.....	31
5.3 Meshing of Fluid Domain.....	32
5.4 Simulation Setup and Post Processing.....	33
5.5 Preliminary Results	35
5.6 Results.....	37
CHAPTER 6.0	51
6.1 Conclusions	51
6.2 Potential Future Work	52

REFERENCES.....	53
-----------------	----

LIST OF TABLES

Table 1: COSO Design Requirements	9
Table 2: System of Equations to be Solved	23
Table 3: FV Design Mesh Independence Study Results	36
Table 4: COSO Design Mesh Independence Study	37
Table 5: FV 2D/CFD Comparison	38
Table 6: FV v COSO Performance Parameters	42

LIST OF FIGURES

Figure 1: Typical GPP Setup	2
Figure 2: Plant Net Power Output as Function of NCG Fraction	4
Figure 3: A Prototype Wound Impeller with Integrated Magnets in Shroud	5
Figure 4: Rotor/Counter-Rotor Pair with VFD Assemblies	7
Figure 5: 11 Stage Prototype Installation	8
Figure 6: 1st 6 Stages of COSO Benchmark Design.....	10
Figure 7: 1D Design Constraint Guide.....	13
Figure 8: Stage Velocity Triangles at Inlet and Outlet	17
Figure 9: IGV Circular Arc Blade Definition	21
Figure 10: R-CR Circular Arc Blade Definition	23
Figure 11: R-CR Main Iteration Loop.....	25
Figure 12: Fluid Domain of COSO Design.....	34
Figure 13: Fluid Domain of FV Design	35
Figure 14: Relative Mach # v. Normalized M.....	39
Figure 15: FV Stage 3 Velocity Vectors at 10% Span	40
Figure 16: Relative Mach # at TE v Normalized Span - 2D/CFD.....	41
Figure 17: Relative Mach # v. Normalized M.....	43
Figure 18: Total and Local Pressure v. Normalized M	44
Figure 19: Entropy v. Normalized M	45
Figure 20: Stage 2 Pressure Rise Coefficient v. Normalized M.....	46

Figure 21: Stage 3 Pressure Coefficient v. Normalized M	47
Figure 22: FV Stage 3 Velocity and Entropy Plots at 50% Span	48
Figure 23: COSO Stage 3 Velocity and Entropy Plots at 50% Span	48
Figure 24: Total-to-Total Pressure Ratio of Full Machine	49
Figure 25: 6 Stages of COSO Design and Equivalent 4 Stages of FV Design	50

KEY TO ABBREVIATIONS

A	Cross-Sectional Area (m^2)
AC	Axial Chord (m)
C	Absolute Velocity (m/s)
CFD	Computational Fluid Dynamics
C_p	Pressure Rise Coefficient
CR1	Counter-Rotor 1
DF	Diffusion Factor
FV	Free Vortex
GPP	Geothermal Power Plant
IGV	Inlet Guide Vane
LE	Leading Edge
LRVP	Liquid Ring Vacuum Pump
M	Mach Number
MW	Molecular Weight (kg/kmol)
N	Rotational Speed (RPM)
NCG	Non-Condensable Gas
P	Pressure (kPa), Power (kW)
R	Mixture Gas Constant (kJ/kg/K)
RANS	Reynolds-Averaged Navier-Stokes
RMS	Root Mean Square
R1	Rotor 1

SST	Shear Stress Transport
T	Temperature
TE	Trailing Edge
U	Blade Speed (m/s)
VFD	Variable Frequency Drive
W	Relative Velocity (m/s)
Z	Number of Blades, Axial Position
a	Speed of Sound (m/s)
c	Blade Chord (m)
c_p	Constant Pressure Specific Heat (kJ/kg/K)
c_v	Constant Volume Specific Heat (kJ/kg/K)
$dH \#$	de Haller Number
h	Specific Enthalpy (kJ/kg)
mf	Mass Fraction
n	Number of Elements
q	Specific Heat Transfer (kJ/kg)
r	Radius (m)
s	Blade Spacing (m)
w	Specific Work (kJ/kg), Circular Arc Geometric Coordinate (m)
y	Circular Arc Geometric Coordinate (m)
Γ	Temperature Ratio
Δ	Change
Π	Pressure Ratio
α	Absolute Flow Angle (deg)

β	Blade Angle, Relative Flow Angle (deg)
γ	Ratio of Specific Heats
ζ	Blade Stagger Angle (deg)
η	Efficiency
ρ	Density (kg/m ³)
σ	Blade Solidity (c/s)
τ	Torque (Nm)
ϕ	Camber Angle (deg), Flow Coefficient
ψ	Loading Coefficient
ω	Angular Velocity (rad/s)
\tilde{e}	Specific Work (kJ/kg)
\dot{m}	Mass Flow Rate (kg/s)
\dot{V}	Volume Flow Rate (m ³)

Subscripts

ax	Axial Component
b	Blade
c	Full Multistage Compressor
hub	Hub
i	Discretization Index
in	Inlet
isen	Isentropic

m	Mean Line
out	Outlet
poly	Polytropic
rel	Relative
shroud	Shroud
t	Total Property
tt	Total-to-Total
u	Tangential Component
1	Stage Inlet
2	Stage Outlet

Superscripts

*	Critical Property
---	-------------------

CHAPTER 1.0

1.1 Introduction to Geothermal Power Plants

With a rising global population there also comes a rise in energy demand and consumption. It is predicted that global energy demand will increase by 56% from 2010-2040 (1). In order to meet these demands, many different sources are available. While the traditional sources (coal, natural gas, and nuclear) are still going to be a large source of energy generation, the need to reduce emissions has driven many renewable sources to be utilized as well. Many of the renewable sources of power are dependent on the cyclic nature of the resource (solar, tidal, and wind) which can be problematic during peak demand periods. Geothermal, however, harnesses the energy locked deep within the molten core of the Earth and can provide a constant source of energy. In the United States, renewable energy sources provided about 12% of the total energy generated in 2012, and less than 3% of that was from geothermal sources (2). That is, geothermal provided less than 0.5% of the total energy generated in the U.S. in 2012. This leaves ample room for expansion both in the U.S. and internationally.

Geothermal energy is typically extracted in areas where extremely hot magma has moved close to the surface. In these locations, it heats the trapped groundwater greatly increasing its energy content. To extract this energy, geothermal wells are drilled where the hot water/steam can be collected and the energy harvested. Afterwards the water can be re-injected back into the earth to keep the supply of hot water going. An example of a typical geothermal power plant (GPP) is shown in Figure 1 (3).

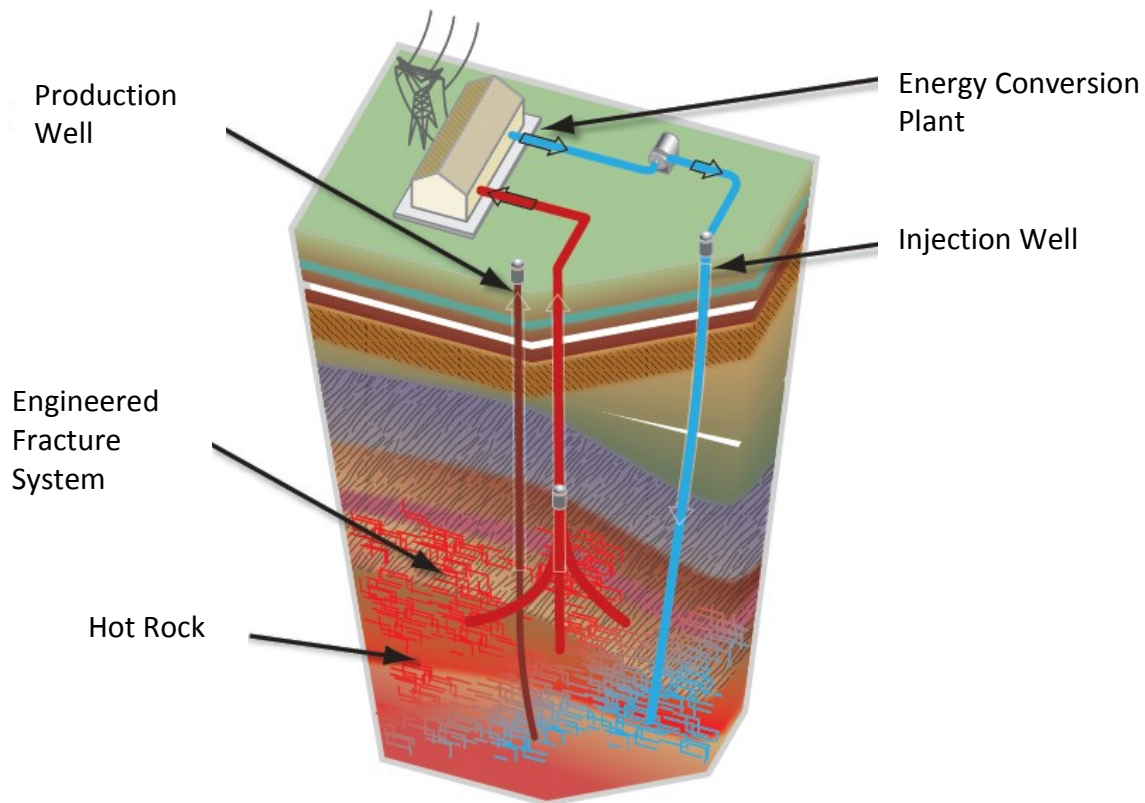


Figure 1: Typical GPP Setup “For interpretation of the references to color in this and all other figures, the reader is referred to the electronic version of this thesis.”

Depending on the location, the geothermal fluid can vary in temperature and chemical composition significantly. For this reason there are three main types of GPPs: dry steam, flash steam, and binary cycle. A dry steam system is used when the geothermal fluid is hot enough to already be dry steam and can be directly used to run a turbine/generator system. When the fluid contains saturated steam/liquid water mixture, a flash steam system is used to flash evaporate the liquid into steam, which is then used to run the turbine/generator system and the remaining liquid water can be sent to the injection well. A binary cycle is used when the fluid is not hot enough to produce enough steam effectively and therefore an auxiliary fluid with a lower boiling point is heated through a heat exchanger by the geothermal fluid and this auxiliary vapor is then used to run the turbine/generator system.

1.2 Issue of NCG Removal and Current Methods

Because most geothermal sources are typically a mix of steam/liquid, flash steam power plants account for 61% of the installed capacity as well as 63% of the energy produced by GPPs (4). Aside from containing a mix of steam and liquid water, the geothermal fluid typically also contains a wide range of other components that exist in the Earth's crust. These contaminants are solids and other gases. Most of these are easily separated off in the flash tank but there are certain non-condensable gases (NCGs) that cannot be easily removed. These are typically mostly carbon dioxide with smaller amounts of ammonia, nitrogen, methane, hydrogen sulfide, and hydrogen (5). If neglected, these NCGs reduce the thermodynamic efficiency at which the turbine can operate. In order to maintain maximum turbine efficiency these NCGs need to be removed. There are several methods currently being used for NCG removal and they are steam jet ejectors, liquid ring vacuum pumps (LRVPs), radial blowers/centrifugal compressors (turbo-compression), reboilers, and hybrid systems. The method or combination of methods used depends on the amount of NCGs that need to be removed.

The most common method is a steam jet ejector which operates using the Venturi effect. However, this method has several areas of concern. They require their own supply of steam to operate which in turn cannot be used to generate electricity. Their capacity is dictated by their size, so multiple ejectors could be necessary, thereby increasing the required space. They can only handle relatively small amounts of NCGs (<3%) and can only achieve efficiencies of 10-15%. A more efficient alternative is NCG removal by turbo-compression, which can easily achieve efficiencies of 75% or higher. A study comparing the performance of a steam jet ejector and a turbo-compressor illustrates the difference in performance as seen in Figure 2, which indicates

that a turbocompression system is not only more efficient, but more effective over a wider range of NCG concentrations (6).

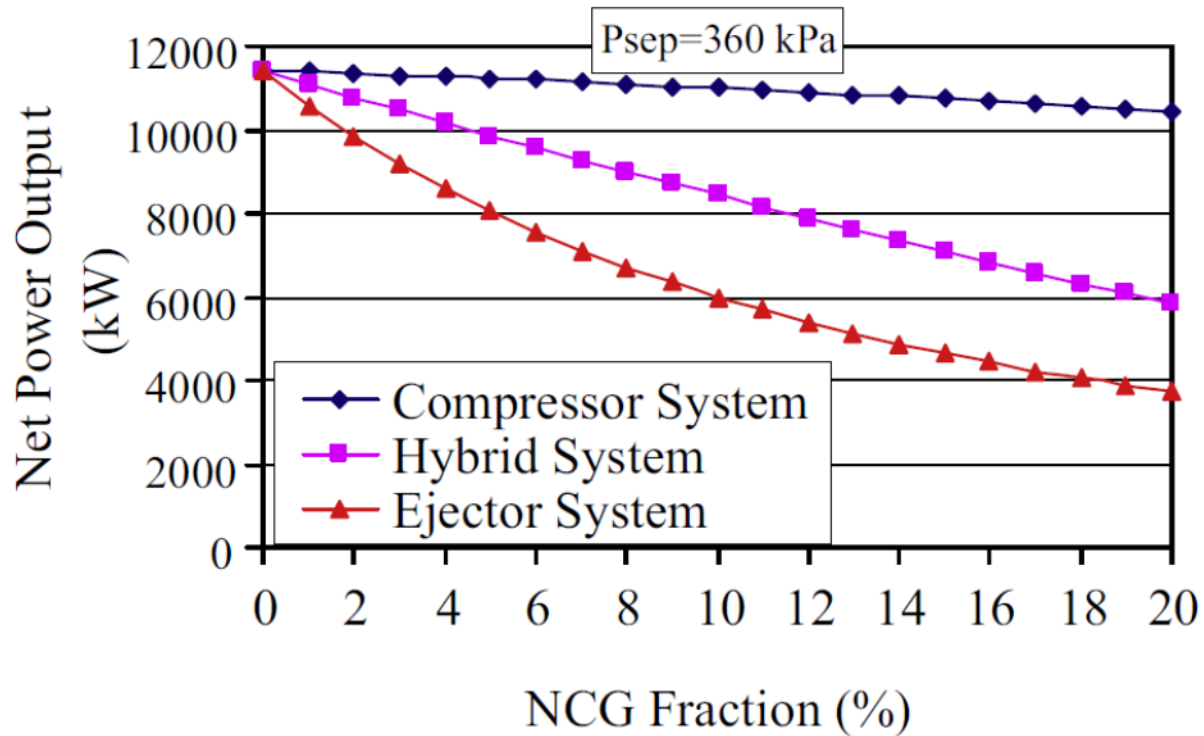


Figure 2: Plant Net Power Output as Function of NCG Fraction

1.3 Proposed Improvement

It is clear that turbocompression is the most logical choice in terms of efficiency and capacity, but this comes at a cost. Installing or converting to this type of system can be both expensive and require large areas of the plant to house all of the components and auxiliary systems. The proposed solution is a multi-stage counter-rotating axial compressor with composite wound impellers (impeller based on patented design by Michigan State University) (7). The composite impellers provide the compressor with a high strength-to-weight ratio (hub, blades, and shroud all one piece) and provide excellent corrosion resistance at the same time.

Integrating magnets into the outer shroud can remove the need for a strong central shaft for torque transmission (see Figure 3). This could remove the need for a central shaft all together (if the bearings could also be adapted to the outer shroud), or the central shaft could be significantly less bulky if its main purpose is simply to support bearings.

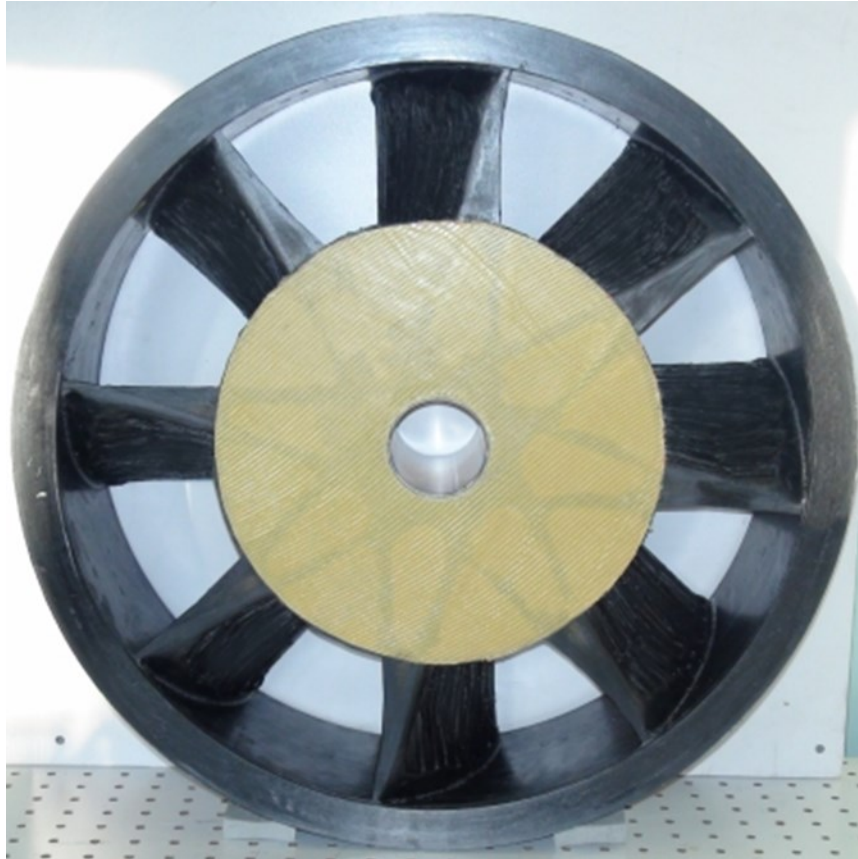


Figure 3: A Prototype Wound Impeller with Integrated Magnets in Shroud

Since the goal is NCG removal and not necessarily maximum pressure ratio, utilizing a multi-stage counter-rotating axial compressor can reduce the size while maintaining the necessary compression and flow capacity versus a multi-stage centrifugal setup. By utilizing counter-rotation, this allows for much higher work potential versus a conventional axial compressor of a comparable volume. Another benefit of counter-rotation is that rotational speeds can be reduced compared to a traditional axial compressor while performing similar work. Also, the

need for stators in each stage is no longer there, allowing for the size to be reduced when compared to a conventional axial compressor where each stage requires its own stator.

The wound impeller design allows for comparatively quick and inexpensive manufacturing as compared to conventional and current composite manufacturing techniques. Conventional impellers are expensive to machine from metals while also producing a lot of waste material. Conventional composite impellers are constructed like the hull of a boat where alternating layers of fiber and resin are layered into a mold and then cured. This process can be very time consuming and also costly. The wound impeller is manufactured by CNC where a continuous fiber that is run through a resin bath is then wound around a set of mandrels that are particular to that specific impeller design. By utilizing a well thought out pattern, there are a wide range of potential patterns/designs that are possible using this technique. The main cost involved is getting the initial mandrels manufactured. After this, impellers are wound, cured, and then the mandrels can be removed and reused. This can greatly reduce the manufacturing costs while producing an impeller of superior strength, lighter weight, and higher corrosion resistance.

CHAPTER 2.0

2.1 Introduction of COSO Application

Currently, an 11 stage counter-rotating axial compressor prototype with wound impellers and integrated shroud magnets is being designed, built, and tested at a single flash GPP located in the COSO volcanic fields in California. In this application, there is an inlet guide vane (IGV) followed by 5 rotor/counter rotor pairs; a guide vane or impeller each constitutes what is defined as a stage. This compressor is to be used as a replacement for the plant's steam jet ejector system. An example of this setup can be seen in Figure 4, which shows a rotor/counter-rotor pair with variable frequency drive (VFD) at the shroud, and in Figure 5, which shows the complete compressor installation.

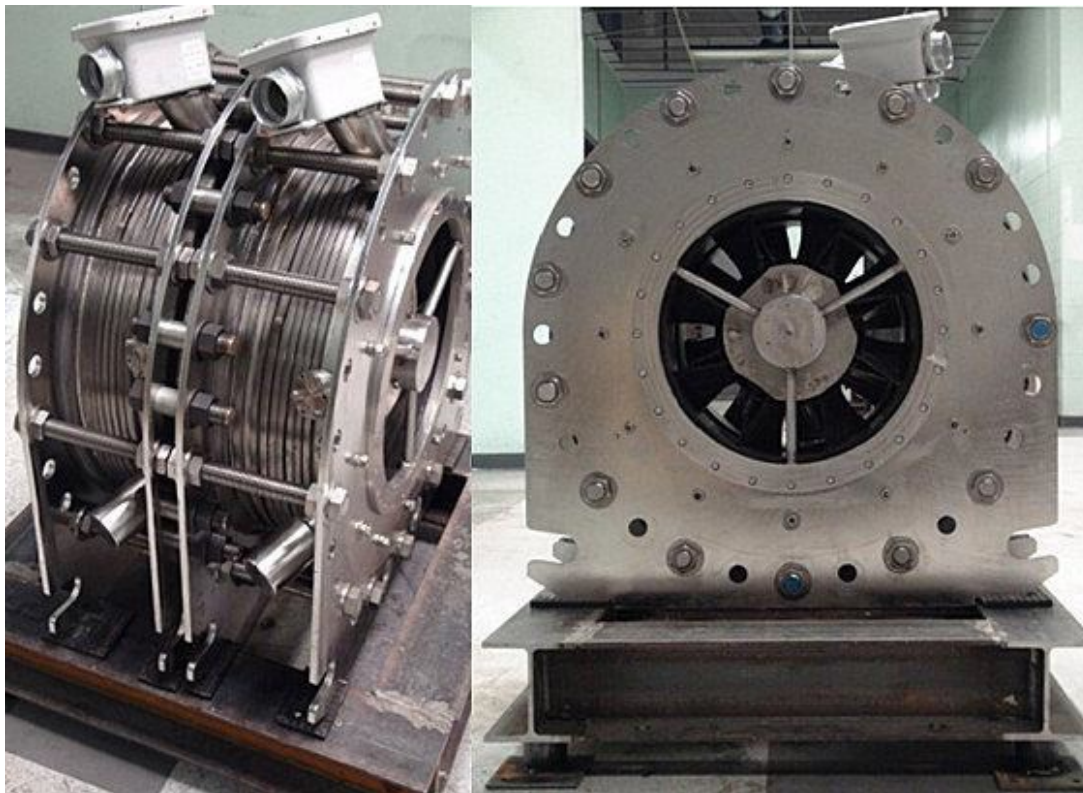


Figure 4: Rotor/Counter-Rotor Pair with VFD Assemblies



Figure 5: 11 Stage Prototype Installation

The specific application of NCG removal imparts its own set of constraints on the requirements of the compressor. More specifically, in terms of the working fluid, mass flow rate (\dot{m}), inlet total pressure (P_t) and total temperature (T_t), and overall total-to-total pressure ratio ($\Pi_{tt,c}$). In order to simplify the initial analysis, and since the NCGs are comprised mostly of carbon dioxide, the working fluid was specified to be a mixture of H_2O and CO_2 . The remaining design specifications, which are mostly geometric, can be found in Table 1.

Table 1: COSO Design Requirements

Property	Units	Value
Mixture MW	kg/kmol	24.50
mf-H ₂ O	-	0.55
mf-CO ₂	-	0.45
γ	-	1.34
\dot{m}	kg/s	2.00
$\Pi_{tt,c}$	-	3.75
$P_{t,in}$	kPa	8.27
$T_{t,in}$	K	309.82
N	RPM	8000.00
IGV r_{shroud}	m	0.26
IGV r_{hub}	m	0.09
Axial Spacing	m	0.12
Z	-	12

2.2 COSO Benchmark Design

Utilizing these baseline parameters, a prototype design was created to enable the COSO plant to begin testing this technology. This design consisted of an IGV of constant hub and shroud radii. The IGV was followed by Rotor 1 (R1) with constant hub and decreasing shroud radius (from 0.26 m to 0.2471 m). This was followed by Counter-Rotor 1 (CR1) which also has a constant hub radius and a decreasing shroud radius (from 0.2471 m to 0.236 m). After this, the remaining rotor/counter-rotor pairs maintain a constant shroud radius of 0.236 m and in turn have increasing hub radii through the rest of the compressor. The rotational speed was kept constant (though alternating in sign to accommodate for the counter-rotation). This design makes use of a constant chord (in both the radial sense and for each rotor or counter-rotor)

and custom airfoil shape for the blade profiles. A model of the first six stages is shown below in Figure 6.

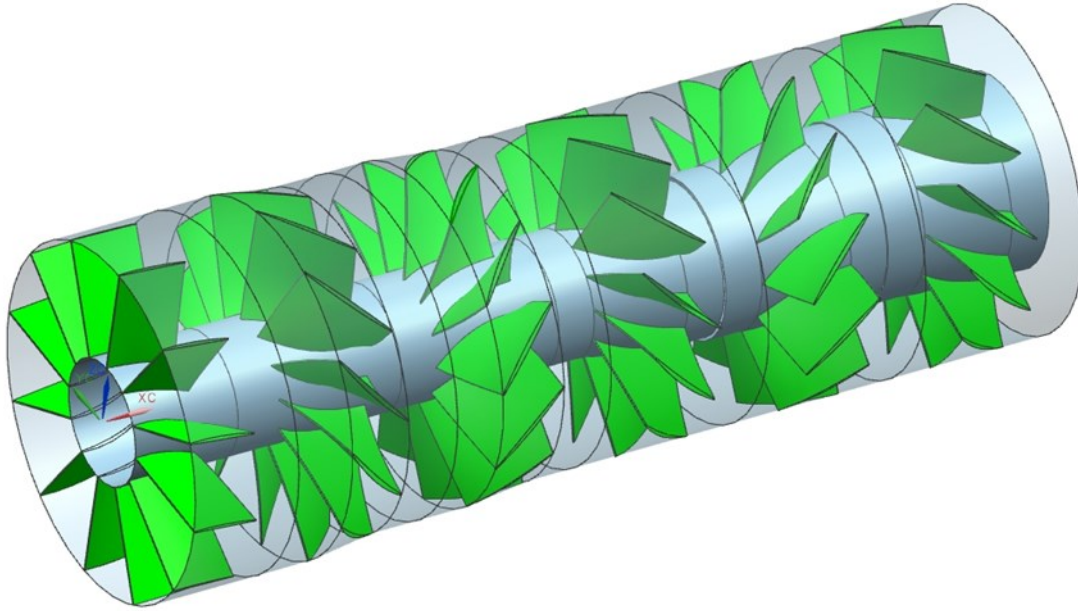


Figure 6: 1st 6 Stages of COSO Benchmark Design

2.3 Scope of Work

The main focus of this thesis will be the design of the first 3 stages of a multistage counter-rotating axial compressor with wound composite impellers and integrated magnets at the shroud (referred to as the FV design). In the benchmark design, both R1 and CR1 have decreasing shroud radii which can unnecessarily add to the difficulty of implementing magnets into the outer shroud. This also reduces the possible work transfer, by reducing the tip speed at the impeller outlets, which translates into reduced pressure gains. Also, while the airfoil shaped blades could be manufactured via the novel wound composite technique, it does present its own set of challenges such as fiber bunching in some areas (for example, at the leading/trailing edges) while being thin in other areas. The constant chord design, which causes

the axial length at the shroud to be less than at the hub, can also contribute to the issue of fiber bunching with the current state of this manufacturing technology. With these potentially problematic areas in mind, basic design goals can be laid out.

The new design must also satisfy the following design requirements:

- Constant tip radius
- Constant axial length (chord not constant in radial direction)
- Constant thickness blades
- Circular arc blades
- Maximize pressure ratio while maintaining efficiency

This will be accomplished by developing a simple 1D design tool in Microsoft Excel. Then this will be expanded into a simple 2D design tool also based in Excel. The 2D design results will then be used as the inputs for creating a 3D CFD model which will be used to validate the design. The COSO benchmark design will also be imported into CFD and the results used for comparison against the new design.

CHAPTER 3.0

3.1 Introduction of Simple 1D Design

The benefits of first performing a simple 1D design is that in this method only a set of algebraic equations are needed (versus partial differential equations) which therefore renders the calculations to be much less complex. When dealing with compressor design, the freedoms that remain for the designer are finely connected to what is given or specified in the design problem. This web of connections can easily cause the design to become over constrained if care is not exercised when deciding what equations can be used where or in which situations. In order to begin constructing the simple 1D design tool, a basic strategy needs to be determined which will be used as guide to ensure that the design remains within the scope of this work as well as making certain that the design does not become over constrained. Figure 7 (below) lays out the basic areas that these constraint issues could originate from and can serve as a reminder of the areas where extra care needs to be taken.

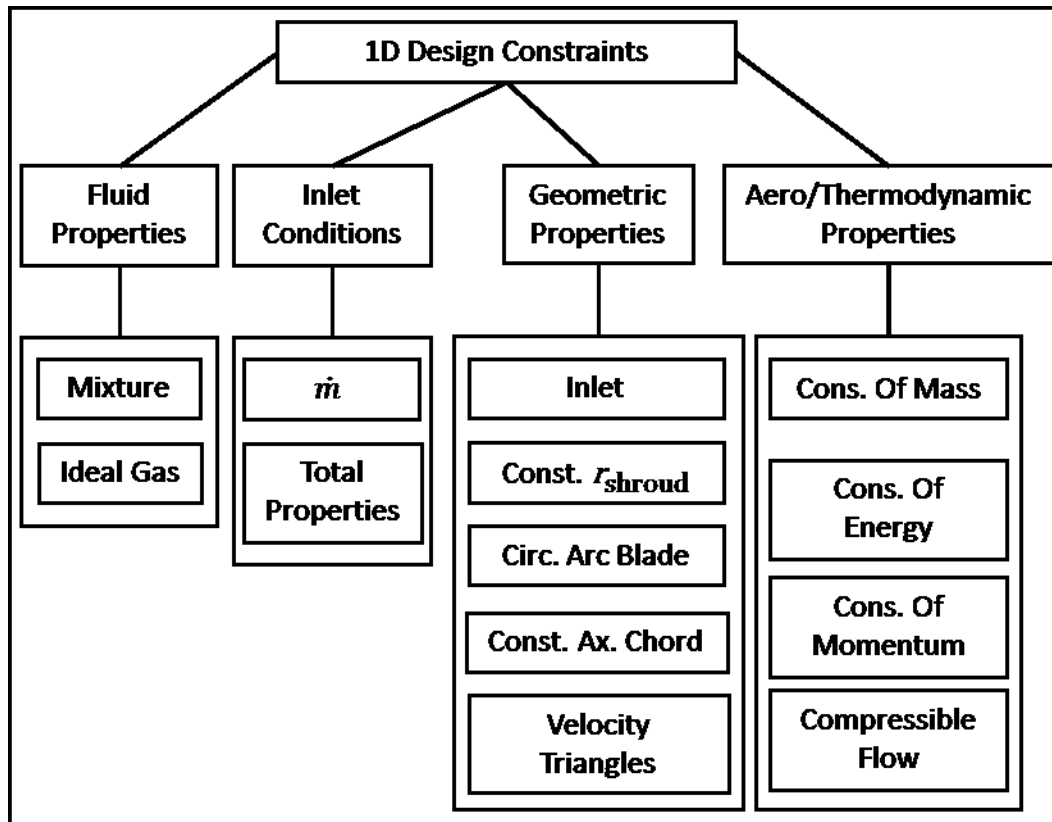


Figure 7: 1D Design Constraint Guide

3.2 Axial Compressor Basics

The goal of a compressor is to increase the pressure of the working fluid by performing work on the fluid. The work is performed by the rotating blades of the compressor impellers. To be able to describe and understand what is occurring during this process several sets of equations are necessary. Several of these are derived using a control volume analysis alongside basic aero and thermo-dynamic laws. The main thermodynamic laws used are ideal gas law, the conservation of mass (continuity), the conservation of energy, and the conservation of momentum. The compressible flow relationships are derived using these laws along with some clever manipulation. Because the design problem required constant thickness blades on a

would composite impeller traditional loss correlations were foregone in favor of a generalized loss through specification of an approximate isentropic efficiency for each stage similar to the method used by Wilcox in (8). The velocity component vector relationships are determined from geometric and reference frame considerations.

The fluid will be treated as an ideal gas meaning that it follows the ideal gas law, which is given as:

Equation 1: Ideal Gas Law

$$P = \rho RT$$

The ideal gas law provides a useful relationship between the pressure, temperature, and density. The pressures and temperatures typically dealt with in compressors are relatively mild when compared with the values necessary for the ideal gas equation of state to start breaking down and no longer remain valid. When using the ideal gas law it is also common to assume constant specific heats (c_p and c_v).

The continuity equation simply states that the mass flow rate into a steady state device (compressors are typically steady state devices) must equal the mass flow rate out of the device and is shown in Equation 2.

Equation 2: Continuity Equation

$$\dot{m} = \rho_1 C_{ax,1} A_1 = \rho_2 C_{ax,2} A_2$$

Next is the conservation of energy, which can be expressed in its simplified form as:

Equation 3: Energy Balance

$$\tilde{e} = \Delta h_t = q - w$$

Where Δh_t is the change in specific total enthalpy (can be thought of as the change in energy of the fluid and is also equal to $h_t = c_p T_t$), q is the specific heat transfer of the system (compressors are assumed to be adiabatic, that is $q=0$), and w is the specific work of the system. This means that the change of energy of the fluid is simply a function of the work done on that fluid. By considering the conservation of angular momentum (Equation 4), it is possible to find another expression for the work.

Equation 4: Conservation of Angular Momentum

$$\tau = \dot{m}(r_2 C_{u,2} - r_1 C_{u,1})$$

If both sides are multiplied by the rotational speed (ω) (where $r^* \omega = U$) and then divided by \dot{m} the expression on the left hand side becomes equal to the specific work. Equating these two expressions for the specific work gives Euler's turbomachinery equation shown in Equation 5.

Equation 5: Euler's Turbomachinery Equation

$$\tilde{e} = \Delta h_t = h_{t,2} - h_{t,1} = U_2 C_{u,2} - U_1 C_{u,1}$$

Inspection of this equation indicates that the work input is directly related to the blade speed (U) and the difference in the tangential velocity of the fluid. The larger the change in C_u , the more work that is done on the fluid and hence larger pressure gains can be realized.

When dealing with moving fluid properties, there are two versions of each property: the local or static and the total or stagnation. The total property accounts for the motion of the

fluid and the local property is as if the reference frame was traveling with the fluid. The exact derivations of these are given in (9) and (10) with the equations themselves given below.

Equation 6: Speed of Sound and Critical Speed of Sound

$$a = \sqrt{\gamma RT}, a_c^* = \sqrt{\frac{2\gamma}{\gamma+1} RT_t}$$

Equation 7: Mach Number and Critical Mach Number

$$M_c = \frac{C}{a_c}, M_c^* = \frac{C}{a_c^*}$$

Equation 8: Total Enthalpy

$$h_t = h + \frac{C^2}{2}$$

Equation 9: Total Temperature

$$T_t = T + \frac{C^2}{2c_p}$$

Equation 10: Ratio of Total to Static Temperature

$$\frac{T_t}{T} = \left(1 + \frac{\gamma-1}{2} M^2\right) = \left(1 + \frac{\gamma-1}{\gamma+1} M_c^{*2}\right)$$

Equation 11: Ratio of Total to Static Pressure

$$\frac{P_t}{P} = \left(1 + \frac{\gamma-1}{2} M^2\right)^{\frac{\gamma}{\gamma-1}} = \left(1 + \frac{\gamma-1}{\gamma+1} M_c^{*2}\right)^{\frac{\gamma}{\gamma-1}}$$

Equation 12: Total-to-Total Isentropic and Polytropic Efficiencies

$$\eta_{tt,isen} = \frac{h_{t,2,isen} - h_{t,1}}{h_{t,2} - h_{t,1}}, \eta_{tt,poly} = \frac{\gamma-1}{\gamma} \frac{\ln(\Pi_t)}{\ln(\Gamma_t)}$$

In multistage compressors, aside from the isentropic efficiency, it is typical to also introduce the concept of the polytropic efficiency as well. The polytropic efficiency accounts for the energy dissipation within a turbine or compressor whereas the isentropic does not. This is why the isentropic efficiency is not conducive for comparing components operating under different conditions. It should be noted that the polytropic efficiency is always going to be larger than the isentropic efficiency in a compressor. As the polytropic efficiency increases (a reduction in energy dissipation), the difference between the two efficiencies reduces as demonstrated in (11).

Another major staple of axial compressor design and analysis are the velocity triangles which describe the velocity vectors in both the relative and absolute frames of reference. General velocity triangles for the inlet and outlet of a rotating stage are shown in Figure 8. It is the absolute components of velocity at the outlet of one stage that are equal to the absolute components of velocity at the inlet of the following stage.

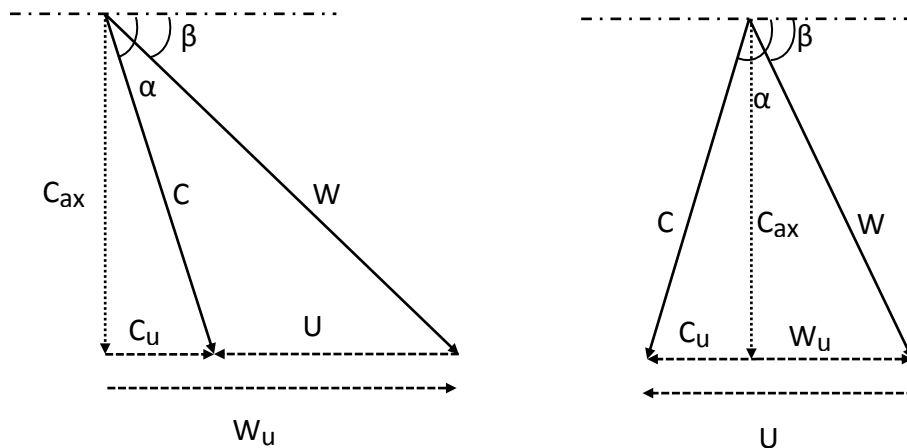


Figure 8: Stage Velocity Triangles at Inlet and Outlet

Through inspection of Equation 5 and Figure 8, it should be seen that since the difference in U between the inlet and outlet is small, the difference in C_u is mostly responsible for the work input and thus the increase in pressure. Logically then, to maximize pressure ratio the blade should provide maximum turning to give the largest difference in C_u . However, in reality if the blades attempt to turn the flow too far, flow separation can begin to occur. Flow separation can lead to compressor stall and large reductions in efficiency so it is important to ensure that this does not occur. Over time several factors were devised to use easily determined quantities to give an indication on when separation and then potentially stall would occur. The simplest was developed by de Haller in 1953 (12) and is given as:

Equation 13: de Haller Number

$$dH \# = \frac{W_2}{W_1}$$

The simplistic nature of this factor makes it quick and easy to use as an indicator of the blade performance, however it is strictly based on the relative flow velocities at the inlet and outlet and does not account for the geometry at all. Lieblein came up with the Diffusion Factor (DF) in 1956 (13) which is similar to the $dH \#$ but with a slight modification. He included de Haller's 1D deceleration ratio and added another term to take into account the relative turning of the flow and its geometry. The relative turning portion is easily identified in the top of the second term (absolute value sign has been included to account for counter-rotation as suggested by Petralanda in (14)). The blade geometry is accounted for through the blade solidity (σ) which is the ratio of the blade chord (c) to the blade spacing (s) (blade spacing is the space between two blades in a 2D cascade). Typically $dH \#$'s must be larger than 0.7. The DF values of greater

than 0.6 typically indicate compressor stall and a sharp drop in efficiency, a value in the range of 0.35-0.55 should ensure that the flow shouldn't separate significantly.

Equation 14: Diffusion Factor

$$DF = \left[1 - \frac{W_2}{W_1} \right] + \frac{|\Delta W_u|}{2\sigma W_1}$$

In order to be able to more directly compare the results of the two compressors of differing design strategy, a non-dimensional pressure rise coefficient (C_p) has traditionally been employed. The pressure rise coefficient deals with the rise in static pressure normalized by the inlet dynamic pressure (dynamic = total - local).

Equation 15: Pressure Rise Coefficient

$$C_p = \frac{P - P_1}{P_{t,1} - P_1}$$

3.3 1D Counter-Rotating Axial Compressor Design Methodology

Due to the rather unusual set of design specifications, an unconventional design methodology needed to be developed which could accommodate for this. Since the IGV has constant hub and shroud radii, and if an isentropic flow is assumed, the given IGV total pressure and temperature can be considered constant through the IGV. Now the total properties, mass flow rate, rotor inlet geometry are known. By specifying a constant axial length as well as circular arc blades, this means that if the blade angles at the inlet and outlet of the rotor are known then this completely specifies the blade angle throughout. With this information it was

possible to step through the rotor satisfying continuity by solving for the requisite hub profile. This same process was then repeated for CR1. Once both the R1 and CR1 designs have been deemed satisfactory the focus was shifted back to the IGV where it was “reverse designed”, that is it was matched to the desired inlet conditions of R1.

The first step that needed to be taken was to discretize the 1D domain (axially). Since the axial length or axial chord (AC) is constant throughout the compressor, no special care is required when switching from IGV to R1 or R1 to CR1. Each domain was discretized equally into $n=15$ elements or $n+1=16$ nodes. Therefore the length per element is AC divided by n . The generalized formula is given in Equation 16

Equation 16: 1-D Discretization

$$Z_i = Z_{i-1} + \frac{AC}{n}$$

With the spatial discretization completed it was then possible to use this in conjunction with some trigonometry to determine the blade angle at each axial node. For a circular arc blade, the inlet and outlet angle are related by the camber angle:

Equation 17: Camber Angle for Circular Arc Blade

$$\phi = (\beta_{in} - \beta_{out})$$

Figure 9 illustrates the circular arc blade under the special condition that β_{in} is equal to 90 degrees (with respect to the tangential versus 0 degrees if it was referenced to the axial direction), which applies to the IGV. Notice that for $\beta_{in} = 90$ the stagger angle (ζ) is equal to $\zeta = \phi/2$.

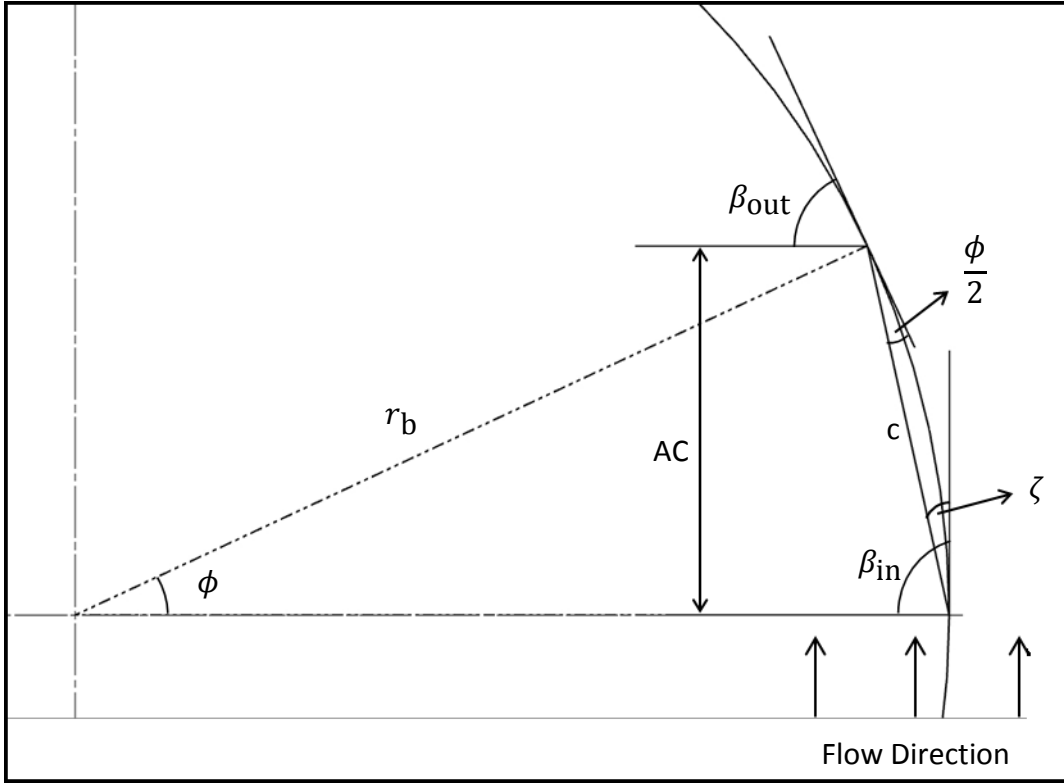


Figure 9: IGV Circular Arc Blade Definition

It should be realized that the radius of the circular blade curvature can be determined via trigonometry:

Equation 18: IGV Blade Radius of Curvature

$$r_b = \frac{AC}{\sin \phi}$$

With r_b and ϕ it is possible to determine the chord length (c):

Equation 19: Blade Chord Length

$$c = 2r_b \sin\left(\frac{\phi}{2}\right)$$

Now solving Equation 18 for ϕ and substituting Equation 16 for AC :

Equation 20: IGV Discretized Camber Angle

$$\phi_i = \sin^{-1} \left(\frac{Z_i}{r_b} \right)$$

and finally inserting this into Equation 17 and rearranging results in:

Equation 21: IGV Discretized Blade Angle

$$\beta_i = \beta_{in} - \phi_i$$

While this was a relatively simple process for the IGV (because of the 90 degree inflow and thus blade angle), it becomes more complex if the specified outlet blade angle is not 90 degrees. This added complexity can readily be seen by comparing Figure 9 and Figure 10.

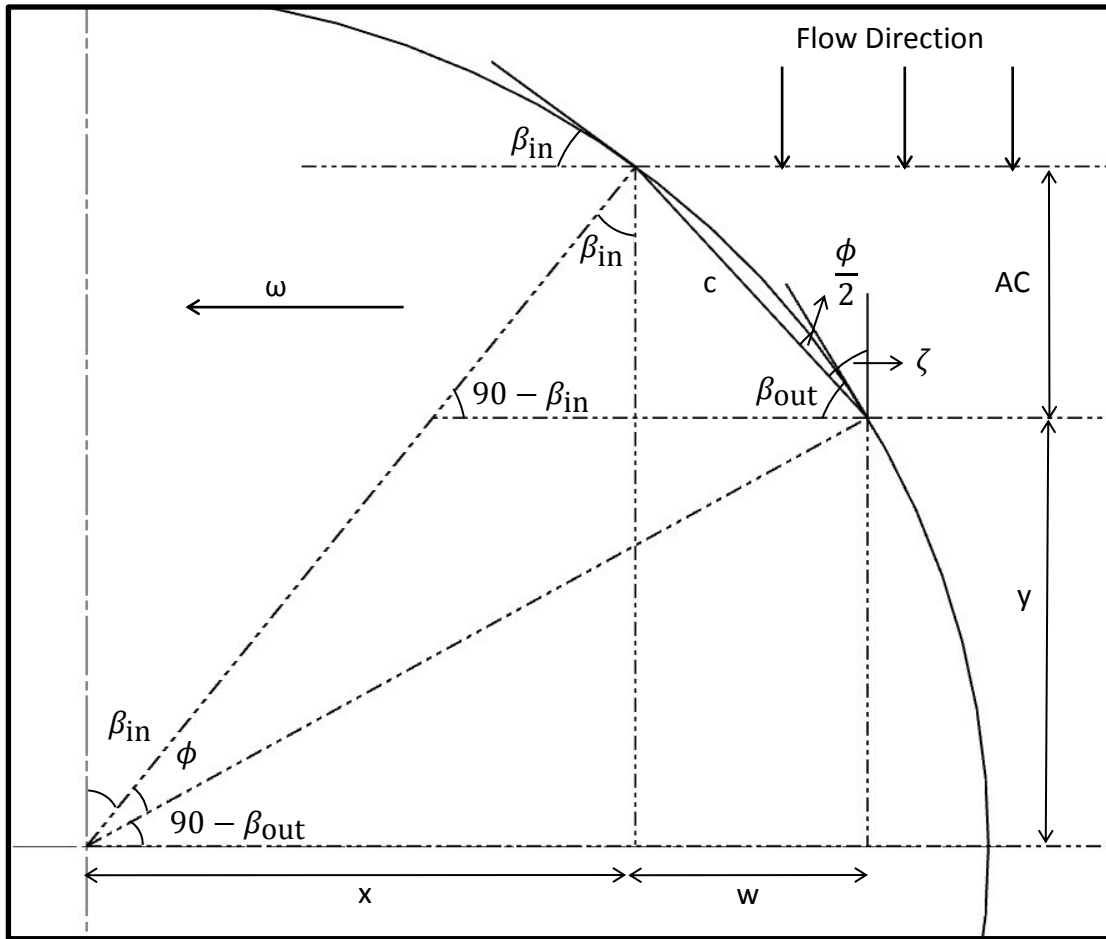


Figure 10: R-CR Circular Arc Blade Definition

There are four important relationships needed to fully determine the blade angle everywhere and are given in Table 2 (Note there are 4 equations and 4 unknowns).

Table 2: System of Equations to be Solved

Formula	Unknowns
$\cos(90 - \beta_{out}) = \frac{x + w}{r_b}$	x, w, r_b
$\sin \beta_{in} = \frac{x}{r_b}$	x, r_b
$\tan \beta_{in} = \frac{x}{AC - y}$	x, y
$\tan(90 - \beta_{out}) = \frac{y}{x + w}$	x, w, y

In order to avoid the tedious nature of solving these through substitution, use of linear algebra in the form of coefficient matrix inversion was chosen instead. The important result is shown in Equation 22, which can then be used in conjunction with Equation 21 to obtain the blade angle at every location. With the blade angles specified everywhere the aero/thermodynamic design process could then be started.

Equation 22: R-CR Discretized Camber Angle

$$\phi_i = \sin^{-1} \left(\frac{(AC - Z_i) + y}{r_b} \right)$$

To begin the design process, aside from specifying β_{in} and β_{out} , an initial guess of C_{ax} (recall $C_{ax} = W_{ax}$) had to be specified. Through the use of the velocity triangle relationships previously introduced in Figure 8, all of the fluid properties and flow conditions can be determined at the inlet node. This includes a calculated \dot{m} which was also specified in the design constraints. To ensure that continuity is satisfied the initial guess of C_{ax} needed to be iterated upon until the mass flows became equal. Now the actual values of the properties have been determined at the inlet of R1.

The remaining nodes however, cannot be solved in this manner because the area is not known at the next node. In order to be able to continue it was assumed that C_{ax} would remain constant throughout the rotor. With this, a $\%r_m$ increase factor was initially guessed (in order to obtain a value of U at the next node, $U = r\omega$) and then later iterated on to satisfy continuity. This process is illustrated below in Figure 11. There are two small differences between the treatment of R1 and CR1 that serves to account for the counter rotation. First, the absolute velocity triangle at R1 outlet is the same as at the inlet of CR1. With C_{ax} , C_u , and U known at

the CR1 inlet, this fully specifies the relative velocity triangle, and therefore β_{in} is calculated rather than specified.

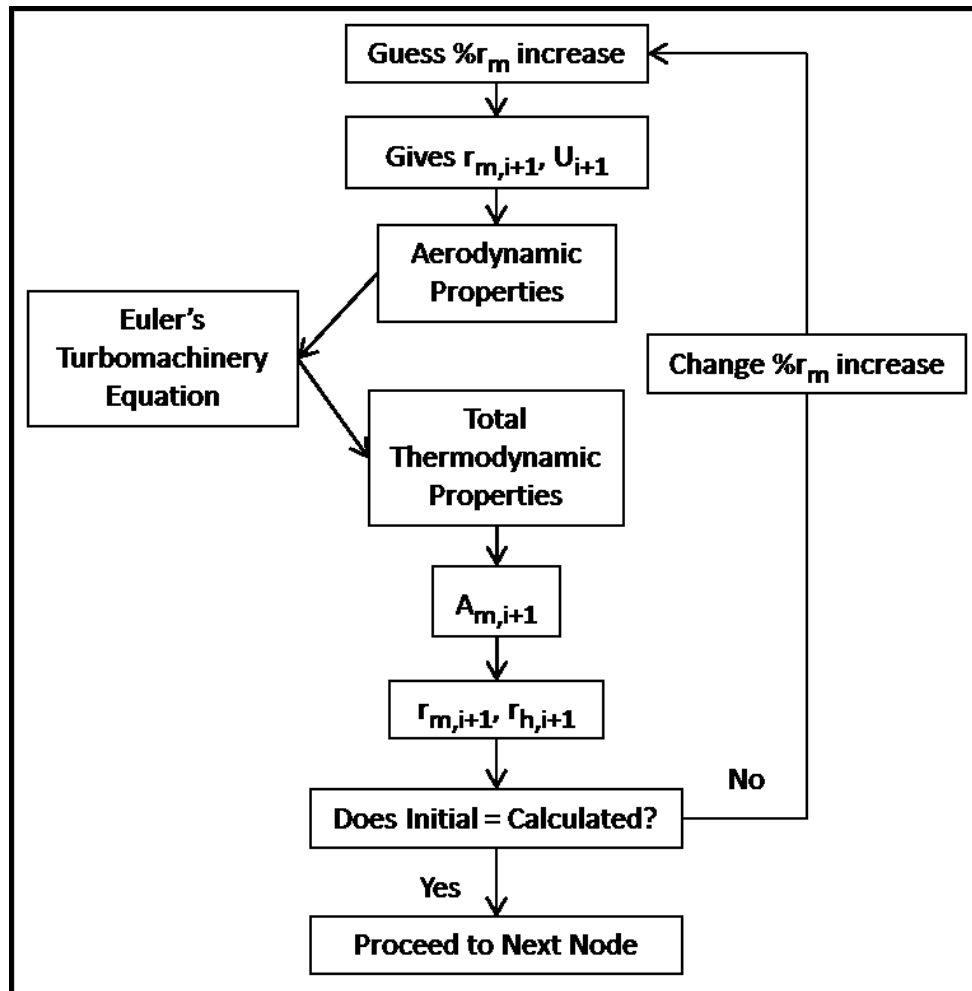


Figure 11: R-CR Main Iteration Loop

R1 and CR1 are now fully defined and solved, so now the IGV can be matched to the R1 inlet. Since the IGV is stationary, the blade angle affects the absolute velocity components rather than the relative velocity components like in the rotating impellers. This can be expressed as $\alpha_{R1,in} = \beta_{IGV,out}$. Now the IGV blade angles are fully specified throughout, and the remaining properties can be solved for by iterating on M_C^* to satisfy continuity at each node beginning at the outlet of the IGV and progressing towards the inlet. Excel/Visual Basic macros

were used to automate all of the iterative steps for each of the stages. Once the macros were functioning correctly, the blade angles could be adjusted to find a combination that provides good pressure rise while keeping parameters like the $dH \#$ and the DF within their limits so as to minimize flow separation, which will decrease the efficiency of the compressor.

CHAPTER 4.0

4.1 Introduction of Simple 2D Design

Although the 1D design process is rather crude in terms of its assumptions and simplifications, it is a vital step of the overall design process for several reasons. First, it serves to help lock certain design constraints into place to help facilitate a smooth transition to the more refined and complex design steps. Secondly, because of the simplifications made, the calculation time is greatly reduced when compared to CFD. This allows for quick baseline optimization before moving on to more advanced design techniques which, due to their increased complexity, have increased calculation times.

Despite the usefulness of the 1D design, it is a mean-line calculation and therefore does not provide enough information to smoothly transition to a 3D design. This is why it is important to expand the calculations from the mean line to the hub and shroud to better define the compressor's geometry. These results will provide the necessary data needed to create a model for CFD.

4.2 2D Counter-Rotating Axial Compressor Design Methodology

In order to make the transition from 1D to 2D, the assumption that there is no radial velocity component must be maintained. The rotational motion imparted on the fluid by the blades causes an inertial force to be generated facing radially outward. The increasing hub radius also contributes to the generation of this inertial force, and if nothing is done to account

for this force, it can introduce a radial velocity component and cause the assumption to become invalid.

One way to deal with the inertial forces is to balance them with a pressure gradient in a simple radial equilibrium. By decomposition of the Euler equation of motion for inviscid flow (in to its cylindrical components) it is possible through several simplifying assumptions to reduce the radial component to (11):

Equation 23: Simple Radial Equilibrium

$$\frac{1}{\rho} \frac{\partial P}{\partial r} = \frac{C_u^2}{r}$$

To determine the static pressure gradient the Bernoulli Equation was used along with the assumptions that P_t and C_{ax} are constant in radial direction. This was then substituted into Equation 23 which transforms it into a separable first order ordinary differential equation. Integration of this new equation results in Equation 24, which is known as the free vortex condition.

Equation 24: Free Vortex Condition

$$C_u r = constant$$

The free vortex condition provides a method to expand the 1D mean line results to the hub and shroud. Before this can be applied, the field needs to be discretized radially, adding the second dimension. Again, 15 elements and 16 nodes were chosen. The elements were distributed based on the mean radius location, which resulted in more elements between the

hub and mean, and fewer elements between the mean and shroud. Each domain has now been fully discretized into an $n \times n$ grid.

Since the 1D mean line results are going to serve as the basis for the 2D calculations, it is not necessary to first solve for R1 and CR1 before the IGV. Assuming uniform inlet properties and using the free vortex condition, all properties and flow conditions can be determined at the first node of the IGV. The remaining IGV nodes are solved similarly as before by iterating M_c^* to satisfy continuity throughout the IGV.

For R1 and CR1, the mean radius at the next node is guess via the $\%r_m$ increase factor as done in the 1D design. The hub radius at this node could then be solved for which then fully specified the radial discretization at this location. With the radii known, the free vortex condition was applied to solve for all the fluid properties at off-mean-line nodes. A new value of the hub radius could be found based on Equation 2. In order to ensure that continuity was satisfied, the difference between the two values of the hub radius at this axial node was iterated to zero by changing the $\%r_m$ increase factor which fully determines the flow field.

It is typical in multistage axial compressors that the hub/tip ratio of the beginning stages is small, which causes the hub radius to change drastically from the inlet to the outlet of the stage. This can cause a radial velocity component to be generated if the hub radius gradient is too extreme, which would violate one of the main assumptions needed to complete this design step. In order to prevent this from occurring, the hub contour was smoothed using a cubic spline.

Up until this point, the design process has assumed inviscid flow to aid in simplifying the calculation process. This is typically a good assumption everywhere except near the hub, shroud, and blade surfaces where in reality viscous effects lead to boundary layer formation. This boundary layer effectively reduces the cross-sectional area of the compressor, which directly affects how much mass flow can fit through (see Equation 2), creating a large discrepancy between the mass flow of the 1D/2D design compared to the viscous 3D CFD simulation. A very simple method was used to determine approximately how much, on average, the boundary layer reduces the cross-sectional area. Through application of boundary layer theory detailed in Pope (15), the boundary layer thickness on each surface was estimated at each axial node. A new value of the cross-sectional area was then determined that included the boundary layer thicknesses. With this area, an approximate, adjusted \dot{m} was calculated. It is this value of the mass flow that must be matched to the 2.0 kg/s that was specified. Since the 1D/2D were originally based on the given \dot{m} it was necessary to go back to the 1D design and increase the \dot{m} . Once the adjusted mass flow rate matched the required value, the design was ready to transition to CFD.

CHAPTER 5.0

5.1 Introduction to CFD

In order to gain a more comprehensive understanding of how the compressor design will perform in reality, a CFD analysis was the next step of the design process. Caution must be exercised however, because CFD results are highly sensitive to the mesh quality as well as the simulation setup (physics, boundary conditions, etc.). The CFD analysis was performed with the ANSYS 14.5 line of software through the use of ANSYS BladeGen, TurboGrid, and CFX modules. First, BladeGen was used to convert the 2D geometry data into an actual 3D model. Next, the simulation domain (fluid flow path) was meshed using the TurboGrid. Lastly, the simulation was setup and ran in CFX utilizing the 2D data to specify the boundary conditions.

ANSYS CFX utilizes a Reynolds-Averaged Navier-Stokes (RANS) solver. This means it employs Reynolds decomposition to break instantaneous velocities into their time-averaged and fluctuating quantities, thus allowing for approximate solutions to the Navier-Stokes equations. The Shear Stress Transport (SST) turbulence model was chosen because it gives highly accurate predictions of onset and amount of flow separation under adverse pressure gradients (16).

5.2 Compressor Modeling for CFD

In ANSYS it is necessary to model and then mesh each stage individually, and then assemble these later. Two models were imported to ANSYS, the COSO benchmark model as well as the 2D design-based model. Each of these had to be imported in a different manner due to the nature of what information was known for each. The COSO benchmark design was imported

via blade profile curves at the hub and shroud. For the new design, the model was constructed by inputting data points to define the annulus, followed by the blade angles at the hub, mean, and shroud positions.

Notice the decreasing shroud radius of the COSO design compared to that of the FV design. Recall from Equation 5 that the work transfer is equal to $U_2 C_{u,2} - U_1 C_{u,1}$. If U becomes less at the outlet due to the decreasing tip radius, then this will reduce the work potential. Also, as specified in the scope of the project, the FV design uses constant thickness blades while the COSO design employs a blade profile. By comparison, the profile used in the COSO design is not drastically different than the constant thickness blades used to reduce manufacturing difficulties with respect to the wound impeller technique. Since the profile differences are not extreme, it should be a relatively safe assumption that they should perform similarly, justifying the tradeoff of a slight decrease in performance for reduced manufacturing difficulty. The CFD results will be able to validate if this assumption holds or not.

5.3 Meshing of Fluid Domain

Since this is a fluid analysis rather than a structural analysis, a model of the fluid domain between the blades is actually what is needed. ANSYS has streamlined the process over the years so that now the 3D compressor models from BladeGen can be linked directly to TurboGrid. TurboGrid then automatically determines the fluid domain from the model rather than it having to be set up manually. ANSYS has also greatly improved the meshing capabilities in recent years. TurboGrid can now automatically generate a relatively high quality mesh very

quickly (high quality means more uniform elements with less warped and stretched elements that would need to be manually corrected using traditional meshing techniques). This automatic meshing option (ATM Optimized) still provides the user the ability to refine the mesh in important areas, such as in the boundary layer and at the leading/trailing edges. Once good parameters have been settled on, it is possible to increase the mesh density through a scaling factor which makes transitioning to finer meshes for mesh independence studies a quick and easy process.

Initially, each stage was meshed with a node count in the range of 400-500,000 nodes, which has shown to be a reasonable mesh size to be able to resolve the potential flow features that occur in an axial compressor (17). In order to validate these results, a fine mesh of approximately 1,000,000 nodes per stage was also created.

5.4 Simulation Setup and Post Processing

At this point, the fluid domains of each stage have been successfully meshed. Now the actual simulation can be setup. The meshes were imported to CFX through CFX-Pre which is the tool used to fully define the simulation physics models, boundary conditions, and solver options. The simulations were modeled as steady state with adiabatic walls, and employed the SST turbulence model. Since each rotor has an equal number of blades, this allows for a periodic boundary condition to be used to reduce the computational domain to only one fluid path for each rotor rather than having to simulate an entire rotor (which would greatly increase the calculation time). Each of the fluid domains that were meshed is shown below in Figure 12

and Figure 13. A P_t and T_t inlet boundary conditions and an \dot{m} outlet boundary condition were chosen since those were specified in the design problem. The time steps chosen varied for the difference mesh densities. For turbomachines, a good time step is typically in the range of $0.1/\omega < \Delta t < 1/\omega$ (the automatic option in CFX-Pre is $0.2/\omega$) (18). Using this as a guide, the automatic time step option was used for the coarser of the two meshes, while the lower limit of $0.1/\omega$ was used for the finer of the two meshes. In order to determine when the solver should stop running, a convergence criterion is used. For a simulation to be considered converged, the normalized RMS residual values for mass and momentum must all become lower than this specified value of 3×10^{-4} .

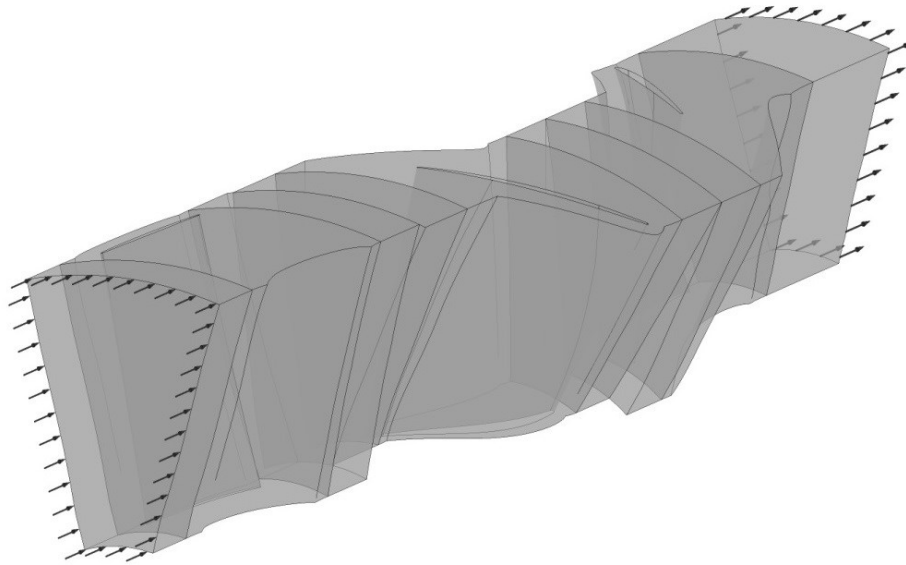


Figure 12: Fluid Domain of COSO Design

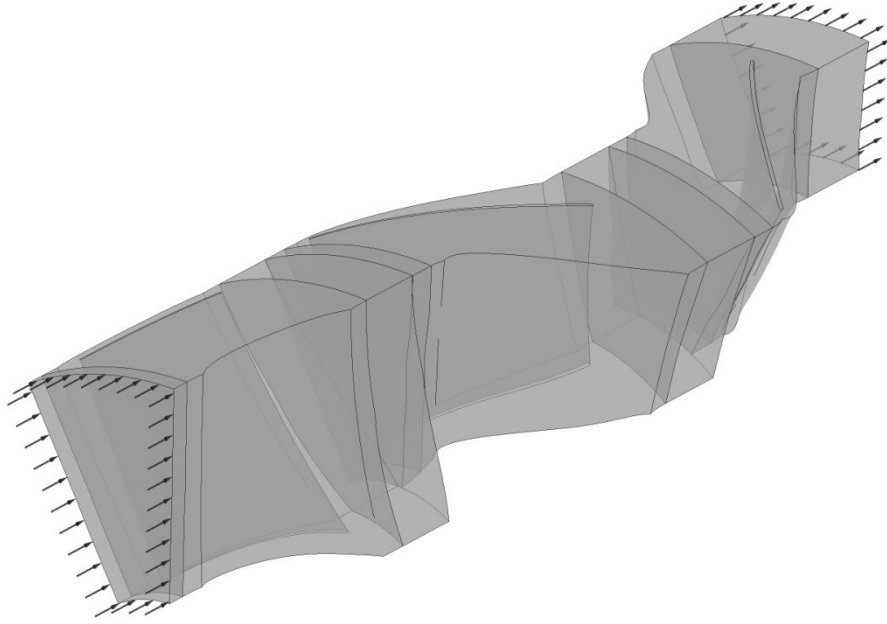


Figure 13: Fluid Domain of FV Design

Once a simulation has converged, the raw data has to be processed in CFD-Post to obtain usable results. CFD-Post provides some premade templates/macros that can be used to generate quantities, charts, tables, and plots relevant to turbomachines, but also provides the freedom for the user to customize the results to their needs.

5.5 Preliminary Results

Before directly comparing the FV design with the benchmark design, it was necessary to ensure the simulation results were realistic. Again, this was accomplished through a mesh independence study. Typically a mesh independence study would require more than two different meshes to determine if the results are mesh-independent or not; however, because the initial mesh was specified based on prior turbomachinery CFD experience (17), the results

were shown to be independent with only one increase in mesh density. The results of this study are shown in Table 3 and Table 4.

Table 3: FV Design Mesh Independence Study Results

FV		Med Mesh	Fine Mesh	%Difference
Rotor				
\dot{e}	kJ/kg	19.13	19.35	1.14
\dot{I}_t	-	1.16	1.16	0.27
$\eta_{tt,isen}$	%	87.23	88.78	1.76
$\eta_{tt,poly}$	%	88.93	90.02	1.22
Counter Rotor				
\dot{e}	kJ/kg	22.38	22.86	2.12
\dot{I}_t	-	1.18	1.19	0.43
$\eta_{tt,isen}$	%	87.23	88.94	1.94
$\eta_{tt,poly}$	%	88.93	90.60	1.86
Machine				
\dot{m}	kg/s	2.01	2.03	0.71
\dot{V}	m ³ /s	25.54	25.72	0.70
\dot{I}_t	-	1.37	1.38	0.48
\dot{I}_t	-	1.10	1.10	0.05
$\eta_{tt,isen}$	%	75.74	76.64	1.18
$\eta_{tt,poly}$	%	89.81	90.53	0.81

Table 4: COSO Design Mesh Independence Study

COSO		Med Mesh	Fine Mesh	%Difference
Rotor				
\dot{e}	kJ/kg	12.45	12.54	0.72
\dot{W}_t	-	1.09	1.09	0.12
$\eta_{tt,isen}$	%	78.80	79.38	0.73
$\eta_{tt,poly}$	%	79.97	80.55	0.73
Counter Rotor				
\dot{e}	kJ/kg	15.48	15.67	1.21
\dot{W}_t	-	1.12	1.12	0.29
$\eta_{tt,isen}$	%	79.77	80.30	0.66
$\eta_{tt,poly}$	%	81.41	81.94	0.65
Machine				
\dot{m}	kg/s	1.97	1.97	0.05
\dot{V}	m ³ /s	24.94	24.96	0.05
\dot{W}_t	-	1.21	1.21	0.41
\dot{W}_t	-	1.07	1.07	0.08
$\eta_{tt,isen}$	%	58.70	59.56	1.46
$\eta_{tt,poly}$	%	77.30	77.96	0.85

If the results vary by more than a few percent, then this is a good indication that the results are not mesh-independent. Looking at Table 3 and Table 4, it can be concluded that the results for both designs are independent of their mesh statistics.

5.6 Results

In order to evaluate the effectiveness of the simple design tool, the 2D results needed to be compared to the CFD results. Comparisons of some basic performance parameters are given in Table 5 .

Table 5: FV 2D/CFD Comparison

FV		2-D	CFD	%Difference
Rotor				
\dot{m}	kg/s	1.98	1.99	0.59
\dot{V}	m ³ /s	25.16	25.28	0.46
$I_{\dot{h}}$	-	1.21	1.16	4.19
\bar{e}	kJ/kg	26.84	19.13	33.54
ψ	-	0.86	0.65	27.96
$\eta_{tt,isen}$	-	81.00	87.69	7.93
$\eta_{tt,poly}$	-	81.88	88.92	8.24
$dH \#$	-	0.71	0.75	6.53
DF	-	0.44	0.37	16.99
Counter Rotor				
\dot{m}	kg/s	1.98	1.99	0.62
\dot{V}	m ³ /s	22.07	22.78	3.16
$I_{\dot{h}}$	-	1.21	1.18	1.87
\bar{e}	kJ/kg	27.22	22.38	19.52.
ψ	-	0.82	0.70	14.66
$\eta_{tt,isen}$	-	81.00	87.23	7.41
$\eta_{tt,poly}$	-	81.88	88.93	8.25
$dH \#$	-	0.71	0.71	0.58
DF	-	0.45	0.44	2.23

The strengths and weaknesses of the simplified design approach utilized in this study were illuminated by comparison of these results. For instance, the method of estimating the average boundary layer thickness and using this to calculate a new area and thus adjusted mass and volume flow rates appear to satisfactorily make the transition without the need for a more complicated profile loss correlation to be implemented. There is a downside of using this method though, because the bulk of the calculations are based on the unadjusted (larger) \dot{m} which effectively over predicts the axial velocity component (which carries over into the other

velocity components and fluid properties). A good example of this is demonstrated in Figure 14 where the 2D M_{rel} line is clearly shifted in the direction of higher velocities. Also, recalling Equation 5 and noting that U should be approximately the same in the 2D and CFD, it is only logical that the larger C_{ax} (and in turn C_u) values would cause the specific work to be over predicted as well.

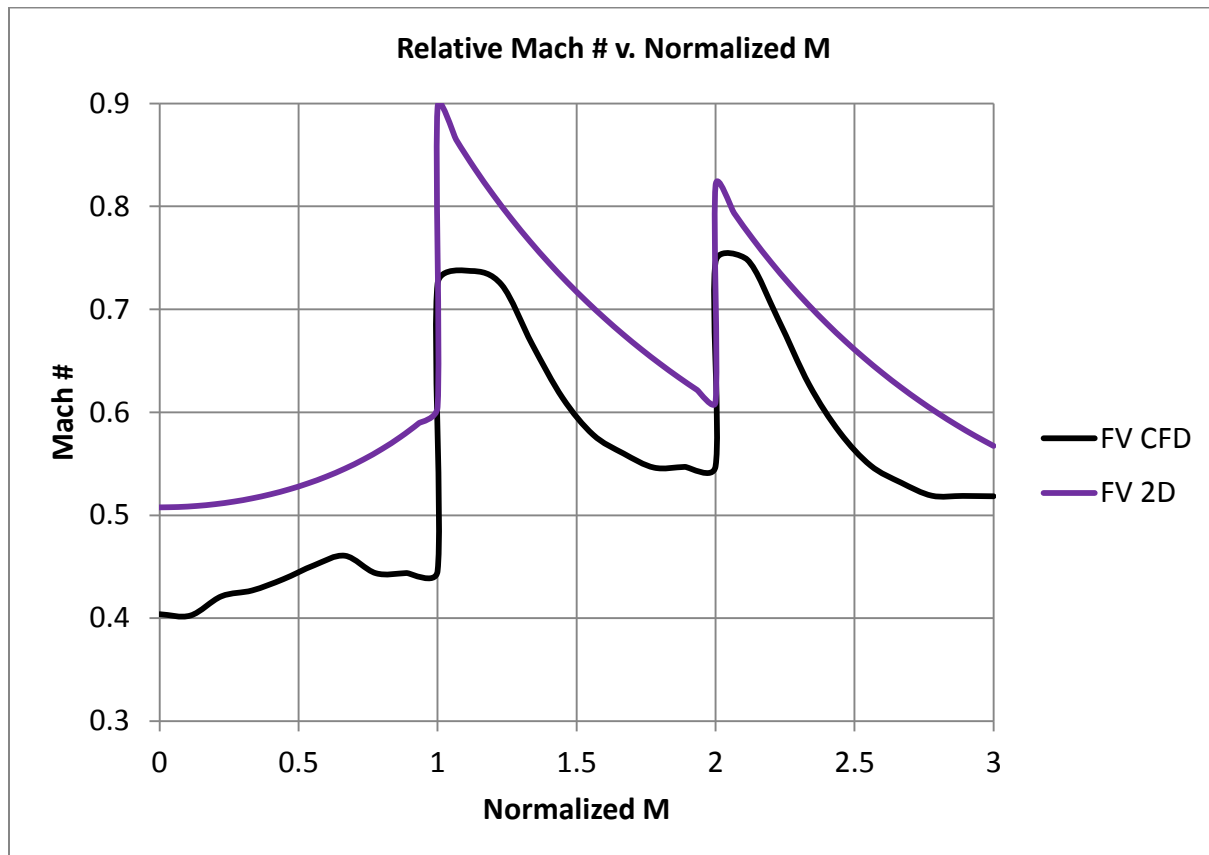


Figure 14: Relative Mach # v. Normalized M

Since the $\eta_{tt,isen}$ was specified in order to account for the losses in the simplified 2D calculation, it was expected this might be an area with some discrepancies. At first it appears as though it was conservatively specified as lower than what it would be in reality. However, the CFD model in its current form has left out the central shaft mounting brackets as seen previously in Figure 4. This was done purposefully in order to initially avoid having to simulate

the full compressor impellers rather than just a single flow path, which greatly reduced the calculation time at this early stage of development. This is also why no attempt was made to go back and use the CFD values to recalculate the 2D design at this point.

Both the dH #'s and DF 's were satisfactorily within their design ranges. Recalling that these parameters were chosen to help ensure that flow separation that could lead to stall and a loss in efficiency was minimal. It would appear that this was accomplished strictly because of the high efficiencies achieved in CFD. This isn't necessarily true though, and can be verified by inspection of a plot of the velocity vectors near the hub of CR1 shown in Figure 15.

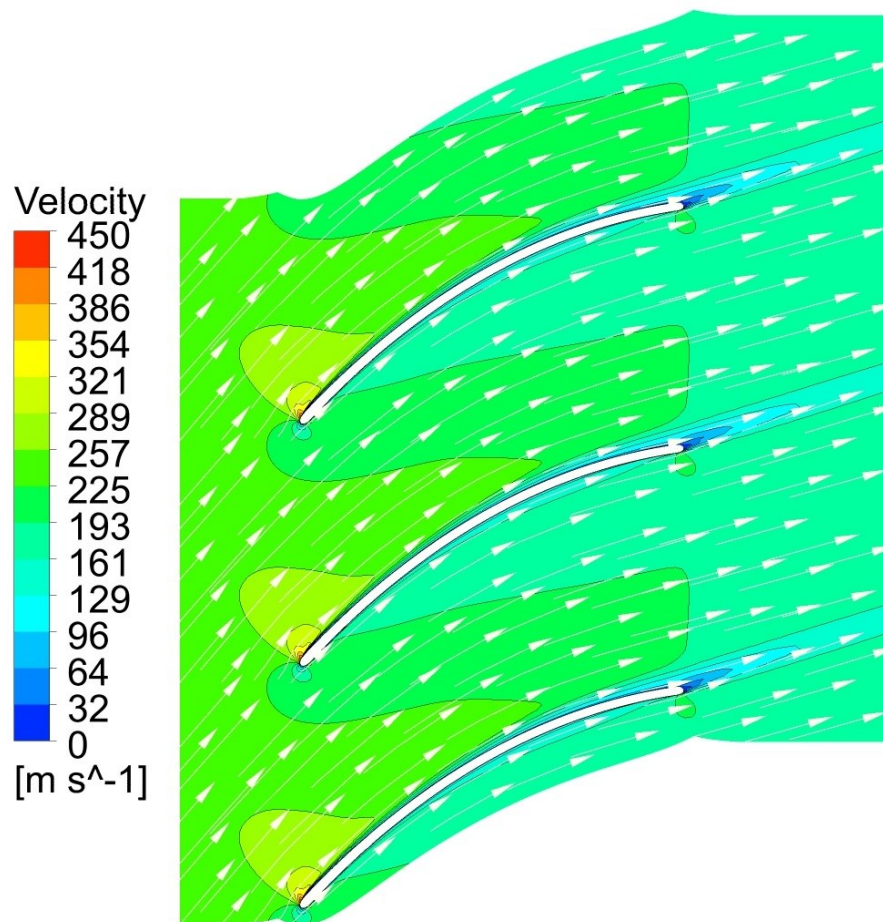


Figure 15: FV Stage 3 Velocity Vectors at 10% Span

Figure 16 shows the relative Mach numbers at the trailing edge for 2D and CFD. The effect of the boundary layer can be seen to reduce M_{rel} near the hub and shroud (the hub is at span 0 and the shroud is at span 1).

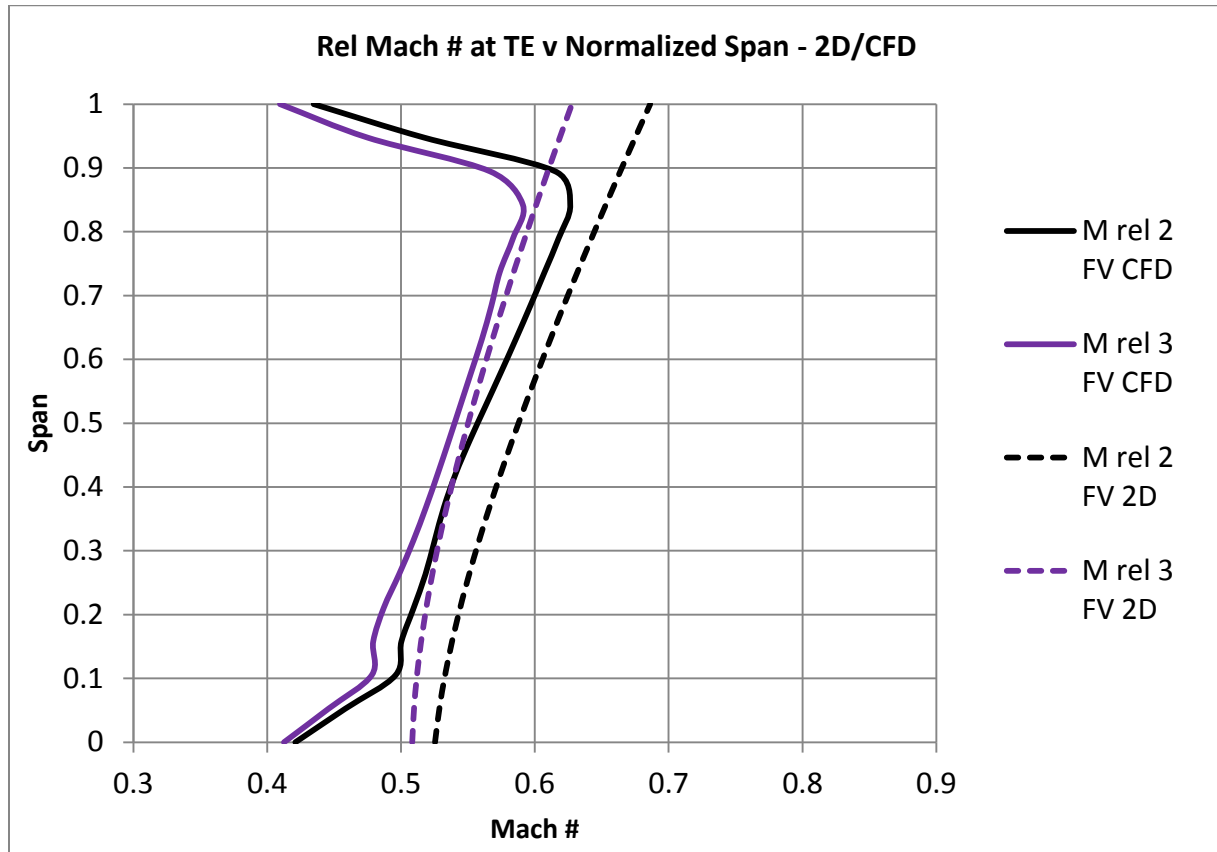


Figure 16: Relative Mach # at TE v Normalized Span - 2D/CFD

At this point it should be noted that while this unique design approach required many techniques and simplifying assumptions that might not be used typically, the results it provided were more than adequate to smoothly transition from a 1D design into successful 3D design. With the FV CFD results validated they could then be compared to the COSO benchmark results.

Table 6: FV v COSO Performance Parameters

CFD Performance Parameters			
		FV	COSO
R1			
\tilde{e}	kJ/kg	19.13	12.45
P	kW	38.11	24.72
τ	Nm	45.49	29.51
Π_t	-	1.16	1.09
Γ_t	-	1.04	1.03
$\eta_{tt,isen}$	%	87.69	78.80
$\eta_{tt,poly}$	%	88.92	79.97
ψ	-	0.65	0.54
ϕ	-	1.00	0.99
$dH \#$	-	0.75	0.82
DF	-	0.37	0.32
CR1			
\tilde{e}	kJ/kg	22.38	15.48
P	kW	44.60	31.03
τ	Nm	53.24	37.04
Π_t	-	1.18	1.12
Γ_t	-	1.05	1.04
$\eta_{tt,isen}$	%	87.23	79.77
$\eta_{tt,poly}$	%	88.93	81.41
ψ	-	0.70	0.72
ϕ	-	1.02	1.14
$dH \#$	-	0.71	0.76
DF	-	0.44	0.39
Machine			
\tilde{e}	kJ/kg	41.52	27.93
P	kW	82.71	55.75
τ	Nm	98.72	82.52
Π_t	-	1.37	1.21
Γ_t	-	1.10	1.07
$\eta_{tt,isen}$	%	75.74	58.70
$\eta_{tt,poly}$	%	89.81	77.30

Through inspection of Table 6 it is shown that the FV design out performs the COSO design in almost every category. The Π_{tt} for the 3 stage machine is almost double that of the COSO design. Some of this increased pressure gain is due to the higher blade speeds that come from keeping the tip radius constant, however because the blade profiles and angles are different, the increase in performance cannot solely be attributed to the constant tip radius.

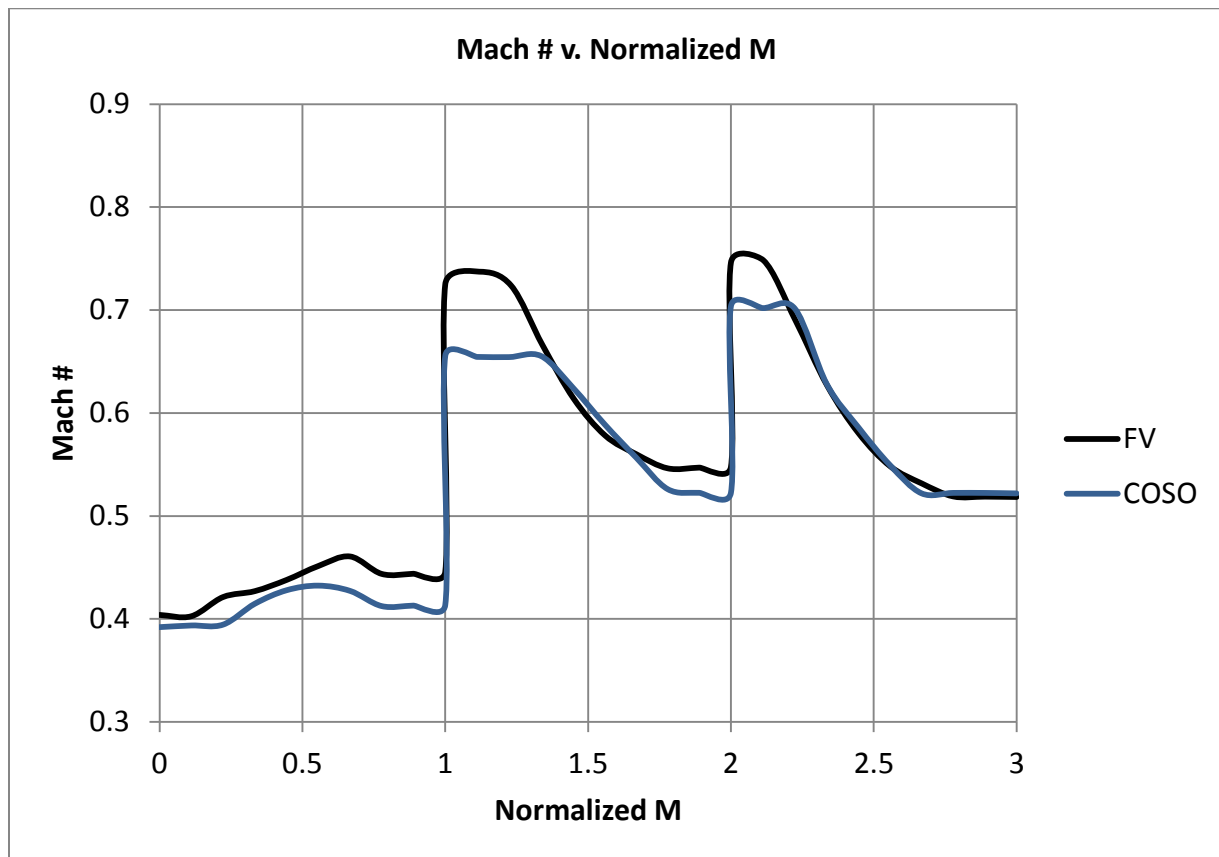


Figure 17: Relative Mach # v. Normalized M

Figure 17 shows the area averaged relative Mach number plotted along the streamwise (or meridional) direction where 0-1 is the IGV, 1-2 is R1, and 2-3 is CR1. The larger the distance between the peak and valley, the more diffusion that occurs between the blades. This was validated by the fact the FV values of the $dH \#$ were lower (larger change in W from inlet to

outlet) than those of the COSO design, as well as the fact that the DF values were higher than those in the COSO design (where higher values of DF indicate more diffusion).

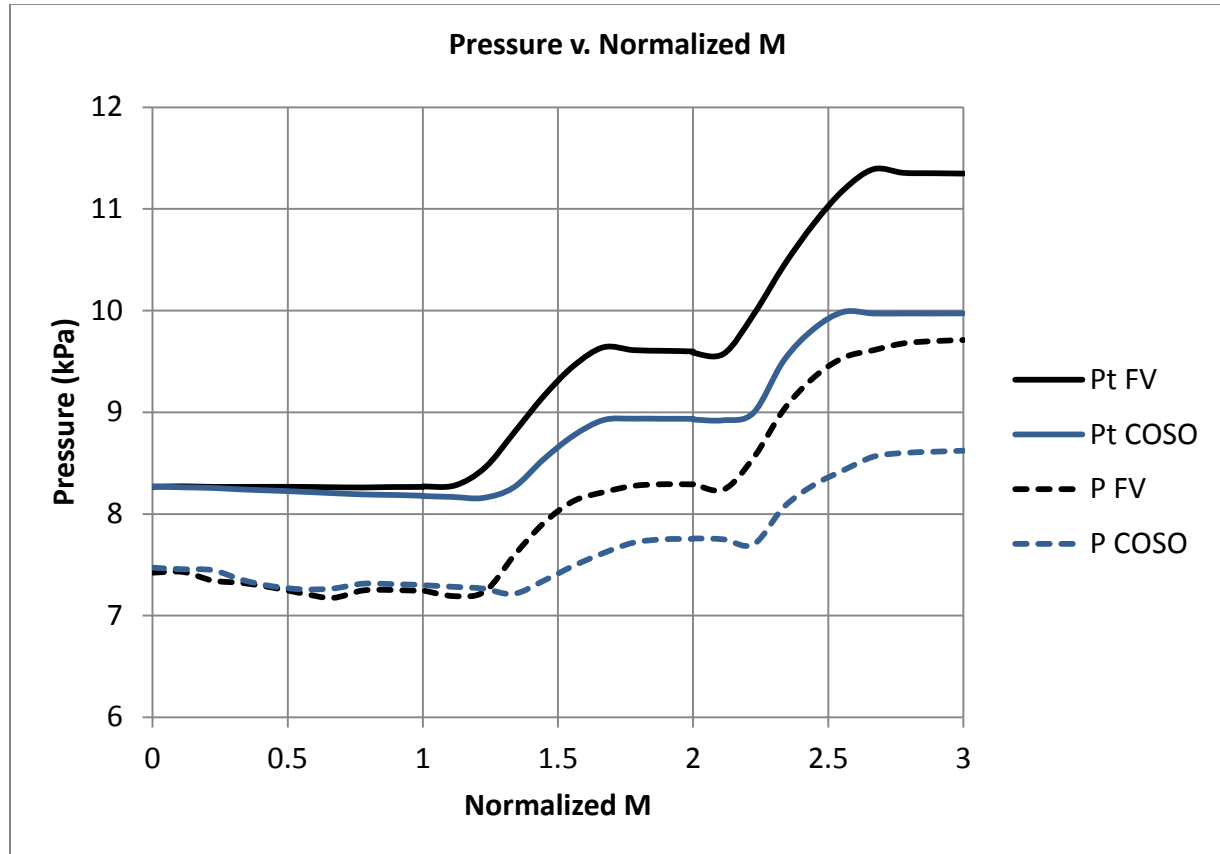


Figure 18: Total and Local Pressure v. Normalized M

Figure 18 shows the total and local pressures and serves to illustrate the difference in pressure gain achieved by each design.

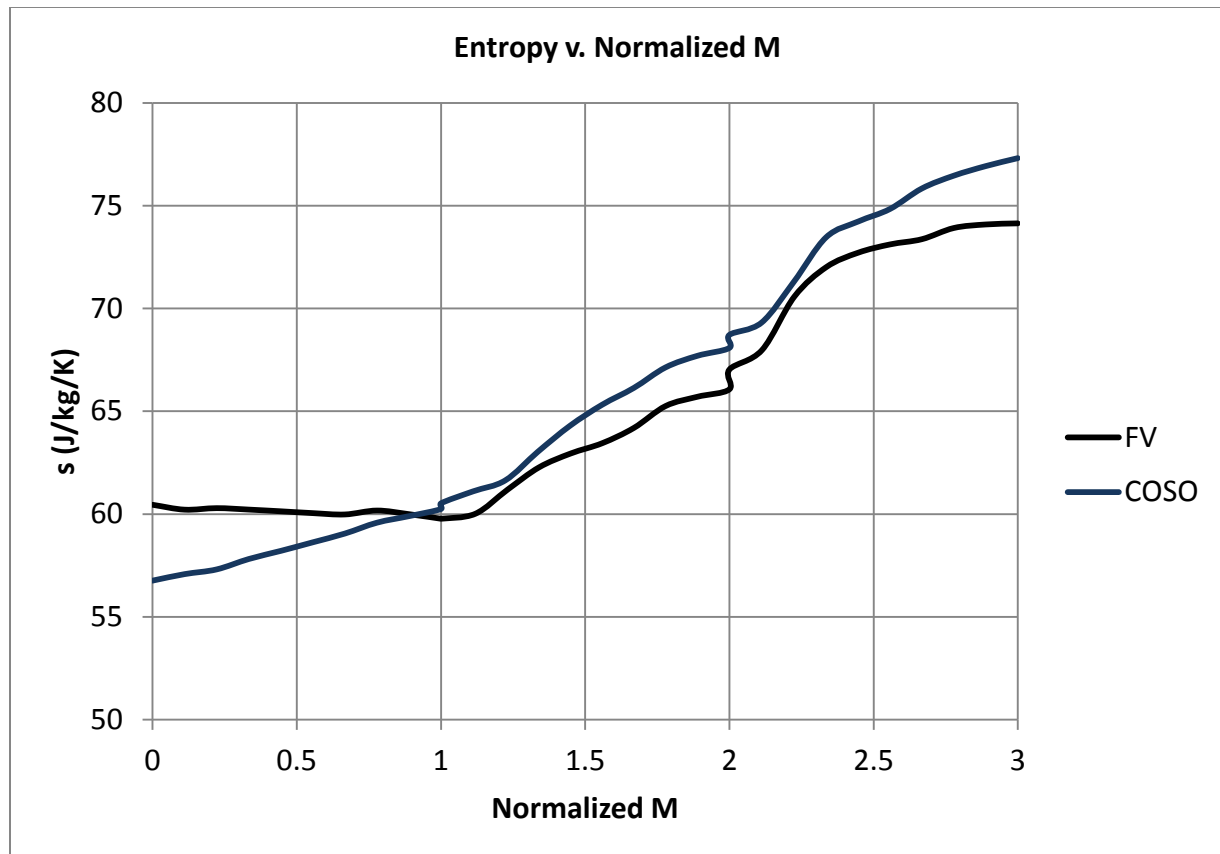


Figure 19: Entropy v. Normalized M

Referring back to Table 6, it can also be seen that the FV design achieved higher efficiencies for both stages and thus also for the machine. These values also help to illustrate the difference between the polytropic and isentropic efficiencies. The isentropic efficiencies for each stage are similar in magnitude, while for the entire machine it is much lower. The polytropic efficiencies do not demonstrate this discontinuity between the stages and the machine and are all of a similar magnitude. It can also be seen that the FV design actually outperformed the benchmark design in terms of efficiency, which was rather unexpected due to the lack of a blade profile. Figure 19 reaffirms this finding by illustrating that the COSO design generated more entropy throughout the compression process.

In order to better compare these two machines it was necessary to make use of the non-dimensional pressure coefficient, C_p . This was plotted along the blade surfaces for both R1 and CR1. These types of charts are called blade loading charts where the bottom portion of the curve represents the suction side and the top portion the pressure side of the blade.

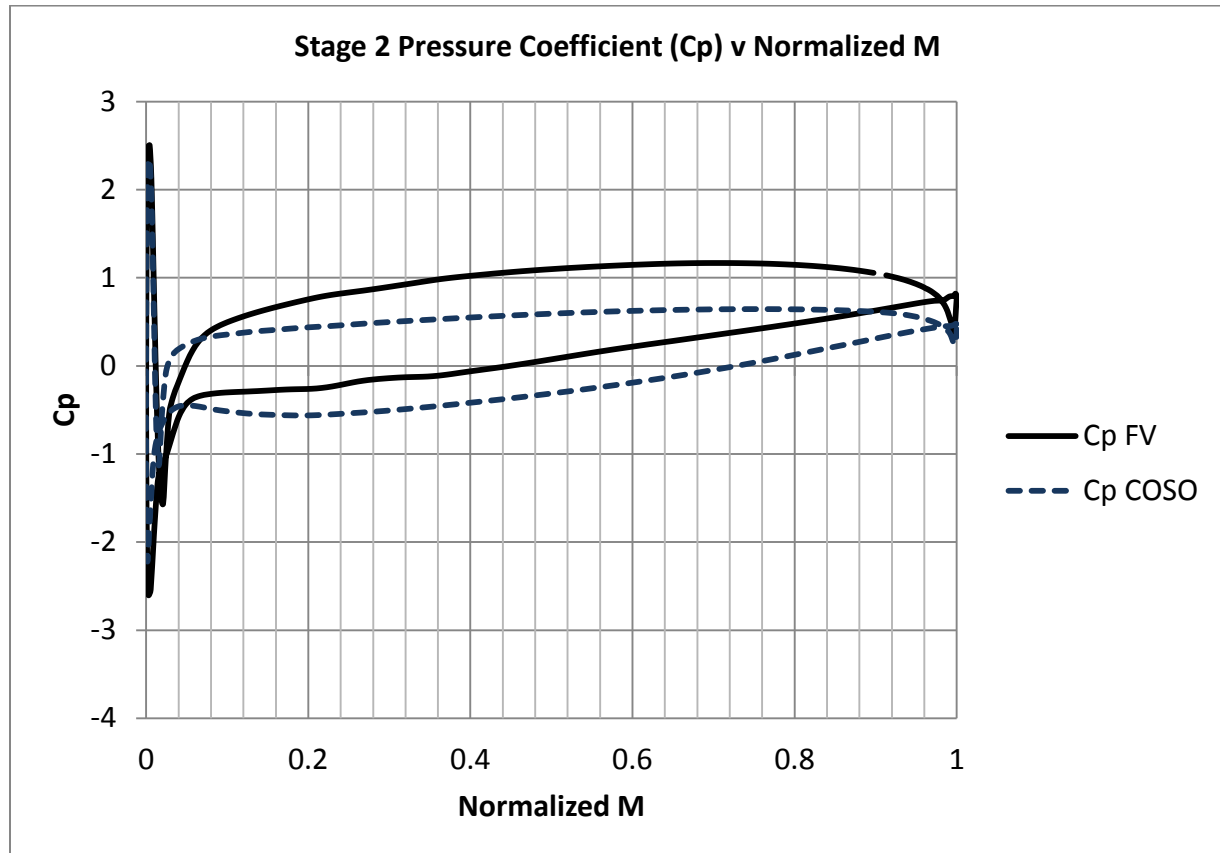


Figure 20: Stage 2 Pressure Rise Coefficient v. Normalized M

Based on the higher pressure ratios achieved by the FV design, it is only logical that the values of C_p would generally be higher, which is the case in both Figure 20 and Figure 21.

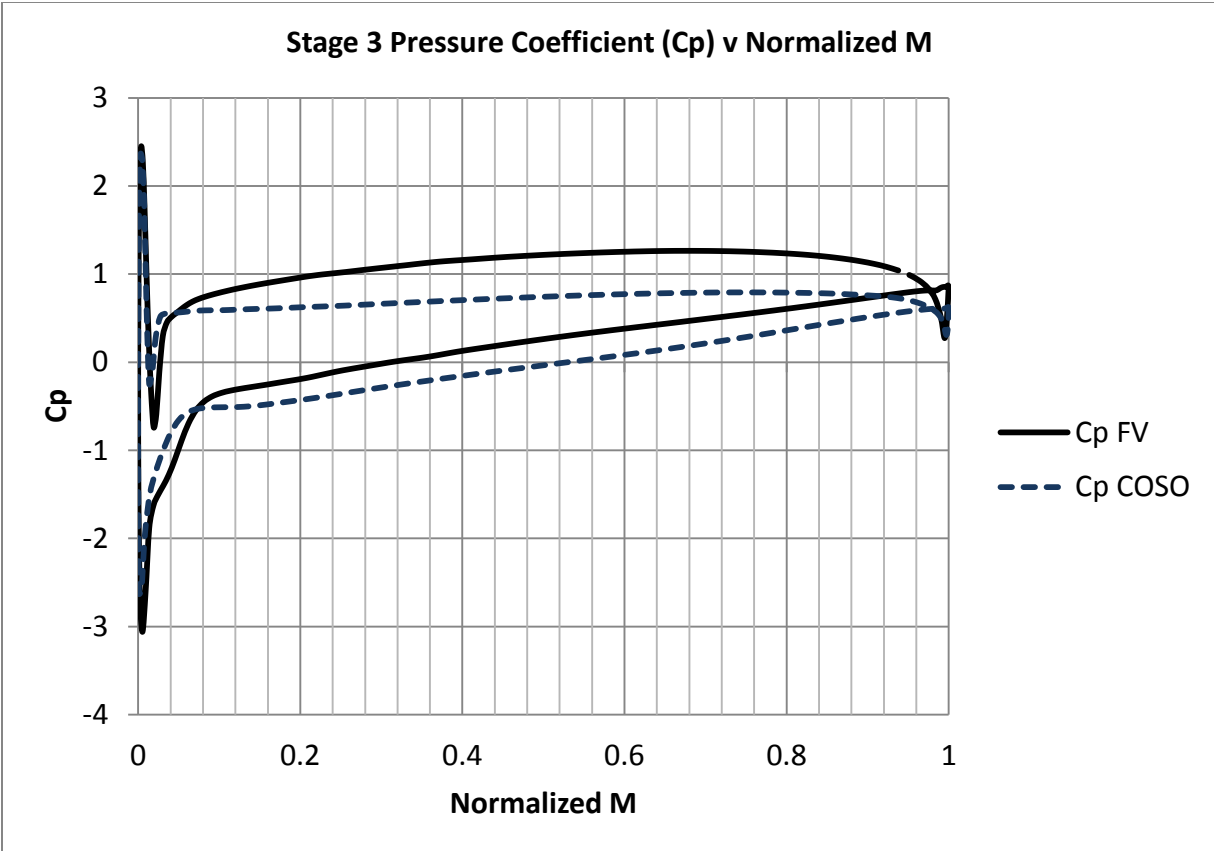


Figure 21: Stage 3 Pressure Coefficient v. Normalized M

For the most part, both of the plots in Figure 20 and Figure 21 are smooth (except at the leading and trailing edges). However, looking at the plot of C_p FV (Figure 21), on the suction side (bottom) immediately after the spike near the leading edge, there is a small disturbance from a normalized M value of about 0.02 to 0.08. Since this artifact occurs in the FV plot and not the COSO plot it was posited that this could be caused by the constant thickness blade profile. In order to investigate this, plots of both velocity vectors and entropy were used (Figure 22 and Figure 23). It can be seen that there is a tiny separation bubble (notice the arrowhead facing in the direction opposed to the core flow direction) just after the leading edge on the suction side of the FV blade which is not present on the COSO blade (18). This is more clearly illustrated in the entropy plot. This is a side effect of the constant thickness blade

profile used in the FV design but is not of major concern because the flow reattaches in just a short distance and therefore has little influence on the overall performance.

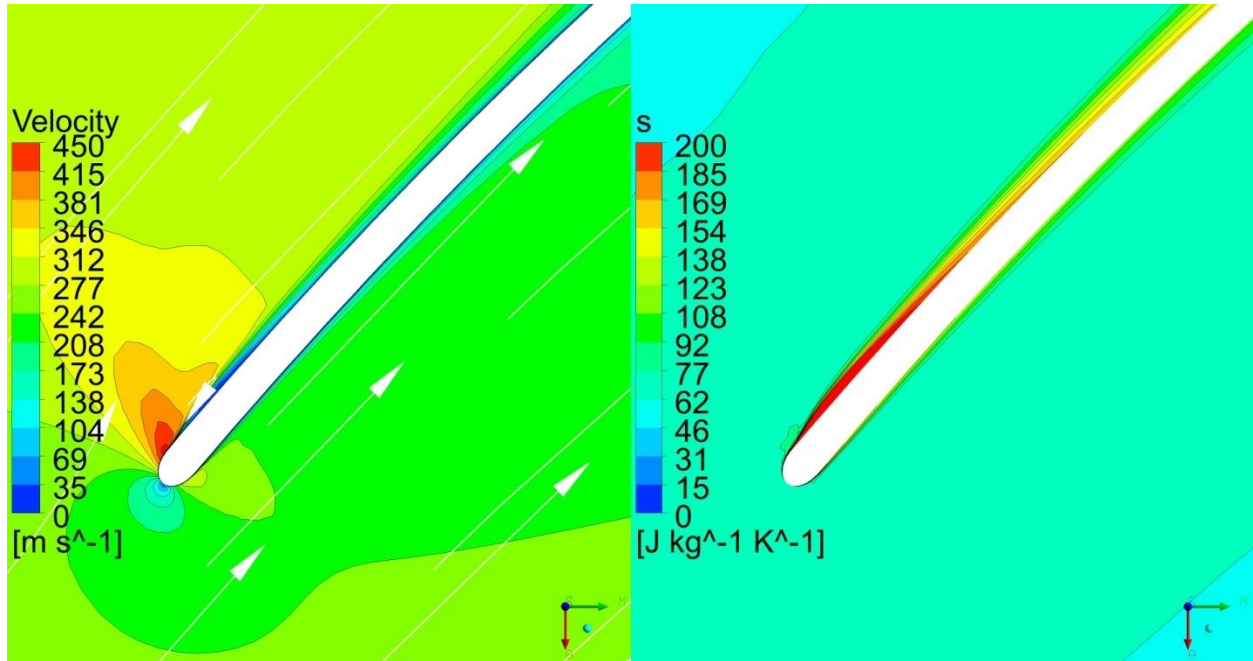


Figure 22: FV Stage 3 Velocity and Entropy Plots at 50% Span

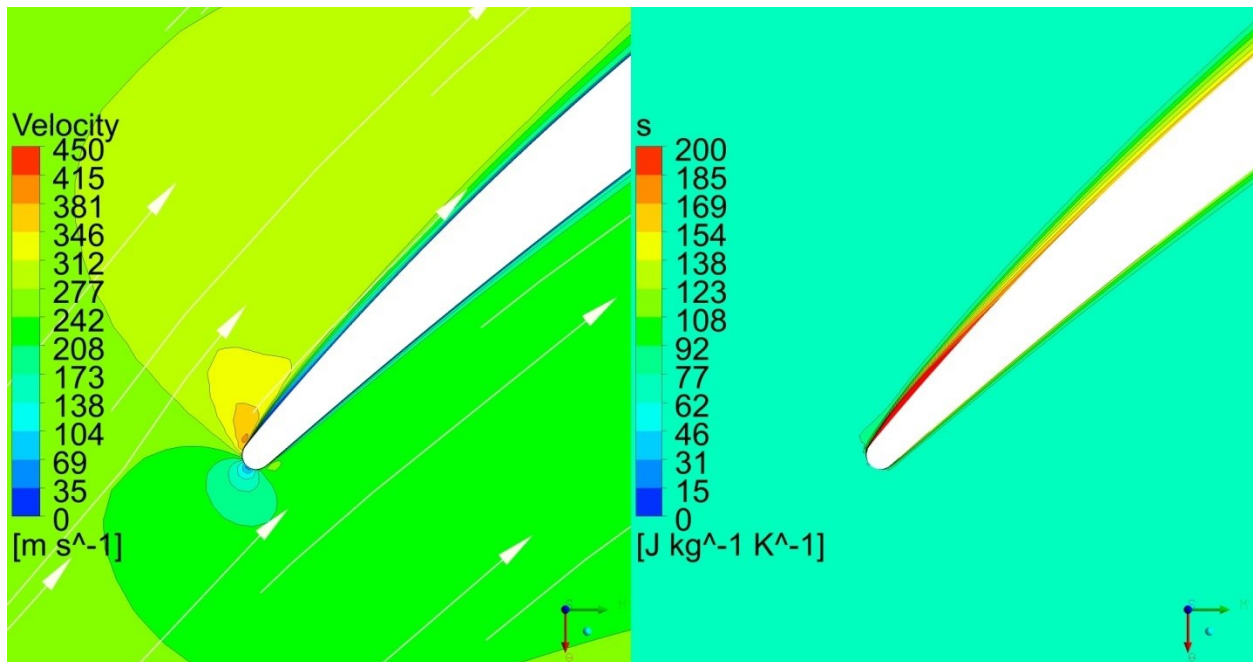


Figure 23: COSO Stage 3 Velocity and Entropy Plots at 50% Span

Despite the extremely simplified 1 and 2D design process, the CFD analysis demonstrated that the design significantly outperformed the benchmark design not only in terms of pressure ratio, but also in efficiency. This means that it would be possible to reduce the number of stages needed to achieve the required $\Pi_{tt,c}$ of 3.75. In fact, assuming the same trend of performance increase would continue if the whole compressor was redesigned, this pressure ratio could be achieved in only 7 stages (as shown below in Figure 24 and Figure 25). This would greatly reduce the initial, maintenance, and operational costs of NCG removal. It would also reduce the space required to house the system, which would make it easier to replace the other less efficient and limited methods of NCG removal.

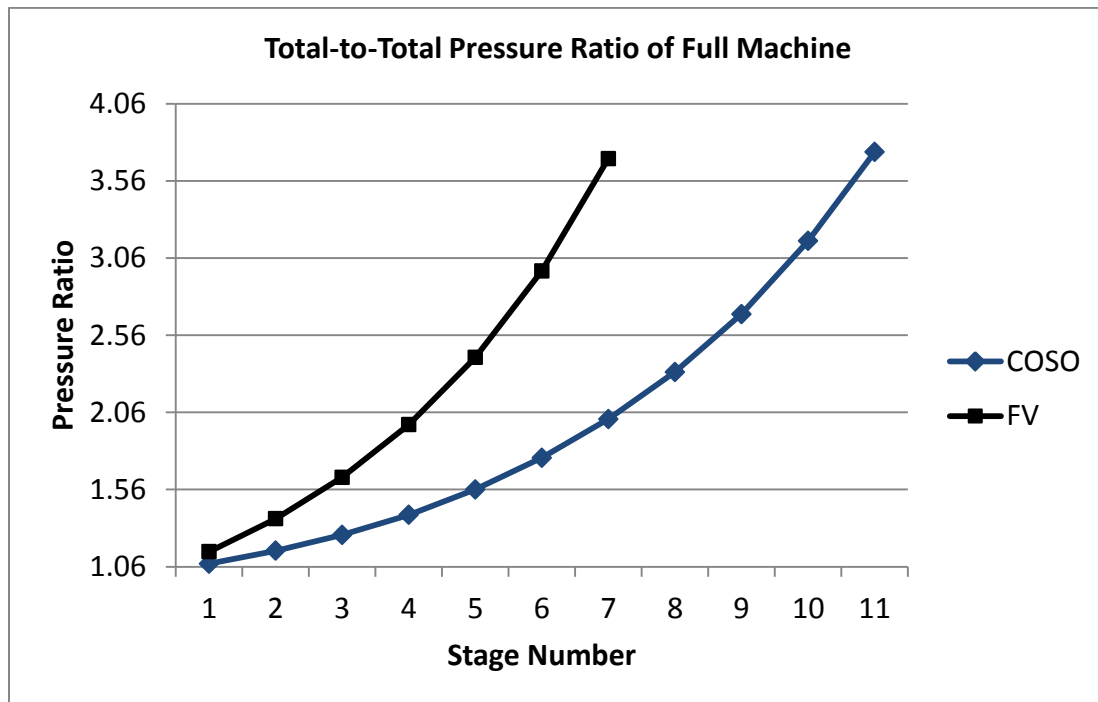


Figure 24: Total-to-Total Pressure Ratio of Full Machine

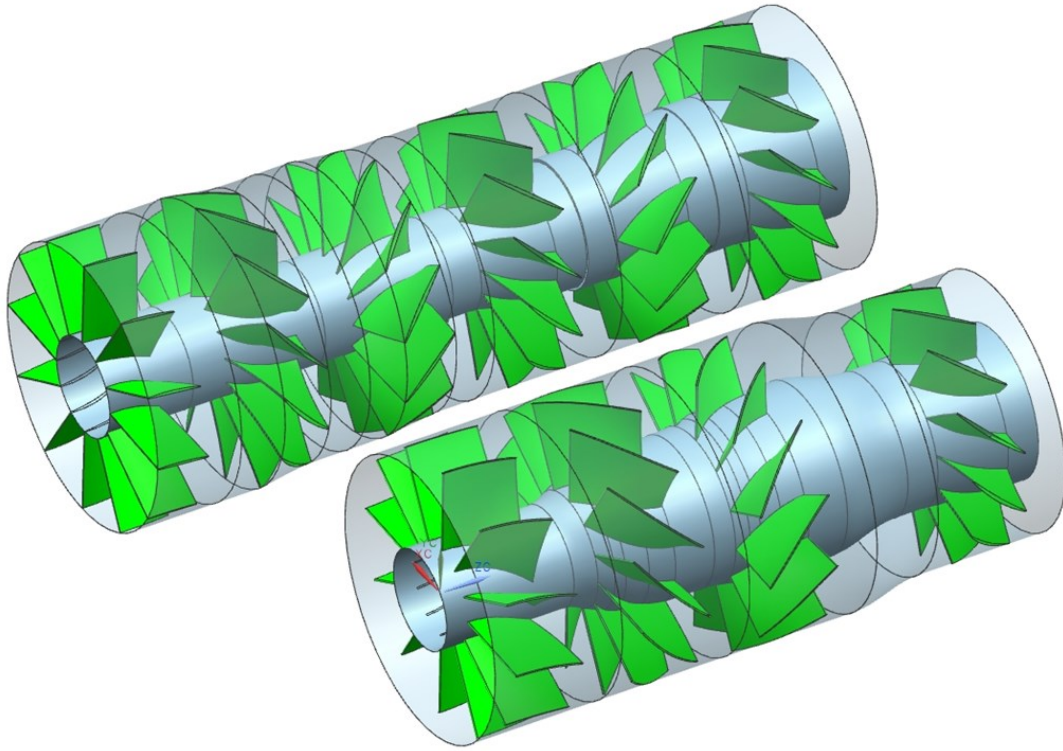


Figure 25: 6 Stages of COSO Design and Equivalent 4 Stages of FV Design

CHAPTER 6.0

6.1 Conclusions

With an increasing demand for energy as well as a need to reduce the negative impacts on the environment from traditional energy sources, the focus in recent years has been shifting towards sustainable and renewable techniques to help meet these demands. While other sources of renewable energy are cyclical or intermittent in their ability to provide power (wind, solar, tidal), geothermal energy sources are not and can provide a constant source of energy. One of the main issues affecting current GPP's performance is the presence of NCG's in the working fluid. Current methods of NCG removal are bulky, expensive, and inefficient. The proposed solution is to use a multistage counter-rotating axial compressor with integrated composite wound impellers.

The focus was on the development of the first 3 stages of this compressor. The scope of the design work was chosen in order to demonstrate that an increase in performance as well as a decrease in manufacturing difficulties, such as fiber bunching, that could occur with utilizing airfoil blades of constant chord was possible to achieve. A simple 1 and 2D design methodology was developed and validated through CFD which demonstrated, when compared to the benchmark design, that it was possible to simplify the design as far as axial compressors are concerned, while still obtaining good flow characteristics and performance results. The 3 stage FV design was shown to be able to obtain a $\Pi_{tt,c}$ of 1.37 and a $\eta_{tt,poly}$ of 89.81% compared to the 1.21 and 77.30% of the benchmark design.

6.2 Potential Future Work

Since the preliminary design and investigation was an overall success, there are several areas that could be focused on for refinement. First, the central axle mounting brackets that were initially neglected to speed up simulation time should be included into the CFD model. This would provide a more realistically prediction of the compressors performance potential. Secondly, the design approach should be expanded to design and simulate the full multistage compressor. Through the addition of the brackets as well as the remaining stages, the performance capabilities and required number of stages can be more accurately determined. Lastly, in order to prove or disprove the CFD results, a prototype of the design should be manufactured and tested.

REFERENCES

REFERENCES

1. **Administration, U.S. Energy Information.** *International Energy Outlook 2013*. Washington DC : U.S. Energy Information Administration, 2013.
2. **Administration, U.S. Energy Information.** *How much of our electricity is generated from renewable sources?* s.l. : Administration, U.S. Energy Information, 2012.
3. **Energy, Department of.** *An Evaluation of Enhanced Geothermal Systems Technology*. Washington DC : U.S. Department of Energy, 2008.
4. *Geothermal Power Generation in the World 2005-2010 Update Report*. **Bertani, Ruggero.** Bali, Indonesia : World Geothermal Congress, 2010. Proceedings World Geothermal Congress. p. 29.
5. **Holm, Alison, et al., et al.** *Geothermal Energy and Greenhouse Gas Emissions*. s.l. : Geothermal Energy Association, 2012. p. 3.
6. *Thermodynamic Assessment of Gas Removal Systems for Single-Flash Power Plants*. **Yildirim Ozcan, N and Gokcen, G.** 15, s.l. : Elsevier, 2009, Applied Thermal Engineering, Vol. 29, pp. 3246-3253.
7. **Mueller, Norbert.** *Woven Turbomachine Impeller*. US 7,938,627 B2 United States, May 10, 2011.
8. **Wilcox, Ward W.** *An Analysis of the Potentialities of a Two-Stage Counter-Rotating Supersonic Compressor*. Lewis Flight Propulsion Laboratory. Cleveland : NACA, 1952. Research Memorandum.
9. **Anderson, John D.** *Modern Compressible Flow with Historical Perspective*. 3rd. s.l. : McGraw Hill, 2004. pp. 28-29,71-83.
10. **Döge, Klaus and Pauer, Reinhard.** *Übungsunterlagen Gasdynamik*. Dresden : Technische Universität Dresden, 1979.
11. **Schoebei, Meinhard T.** *Turbomachinery Flow Physics and Dynamic Performance*. Second and Enhanced Edition. New York : Springer, 2012. pp. 131-133,239.

12. **de Haller, P.** *Das Verhalten von Tragflugelgittern in Axialverdichtern und in Windkanal.* s.l. : Bernstoff-Warmer-Kraft, 1953.
13. **Lieblein, Seymour, Schwenk, Francis C. and Broderick, Robert L.** *Diffusion Factor for Estimating Losses and Limiting Blade Loadings in Axial-Flow-Compressor Blade Elements.* Lewis Flight Propulsion Laboratory. Cleveland : NACA, 1953. Research Memorandum.
14. **Petralanda, Naiara.** *Design and Numerical Evaluation of a Counter-Rotating Compressor in the Absence of Boundary Layer Control: Part I.* Daytona Beach, Florida : Embry-Riddle Aeronautical University, 2008. UMI Number: EP32110.
15. **Pope, Stephen B.** *Turbulent Flows.* New York : Cambridge University Press, 2011.
16. *Zonal Two Equation $k-\omega$ Turbulence Models for Aerodynamic Flows.* **Menter, F. R.** Paper 93-2906, 1993, AIAA.
17. Best Practice Guidelines for Turbomachinery CFD. *CFD Online.* [Online] http://www.cfd-online.com/Wiki/Best_practice_guidelines_for_turbomachinery_CFD.
18. **Cumpsty, N. A.** *Compressor Aerodynamics.* Malabar : Krieger Publishing Company, 2004. pp. 137,152-153,327.